Electronic Supplementary Material (ESI) for Energy & Environmental Science.

Supplemental information

An integrated Janus hydrogel with different hydrophilicities and gradient pore structures for high-performance zinc-ion batteries

Kaiyue Zhu, Xiling Niu, Weili Xie, Hanmiao Yang, Weikang Jiang, Manxia Ma, Weishen Yang

This PDF file includes:

Figure S1 to S47

Table S1 to S3

Captions for Movie S1

References

Other Supplementary Materials for this manuscript include the following:

Movie S1

Synthesis of the PAZPM hydrogel electrolyte

AM, Zn-AC, NIPAM, MBAA, $ZnSO_4 \cdot 7H_2O$, APS and TEMED were dissolved and mixed in distilled water under a nitrogen atmosphere, after which the mixture was injected into the mold. Finally, the PAZPM hydrogel electrolyte with 1 M $ZnSO_4$ was obtained by free radical copolymerization at 60 ℃ for 2 h. The monomer compositions of the PAZPM hydrogels with different amounts of NIPAM are summarized in Table S1.

Synthesis of $(NH_4)_2V_{10}O_{25} \cdot 8H_2O$ (NVO) powders and cathode

$(NH_4)_2V_{10}O_{25} \cdot 8H_2O$ (NVO) was prepared via a hydrothermal method. Briefly, NH_4VO_3 (1.1724 g) was dissolved in 140 mL of deionized (DI) water under stirring at 60 ℃. Then, SDS (0.0600 g) and $H_2C_2O_4$ (1.3506 g) were gradually added to the mixture under stirring for 2 h. Subsequently, the mixture was transferred to a Teflon-lined stainless-steel autoclave and maintained at 130 ℃ for 10 h. The obtained products were collected and washed three times with DI water and anhydrous ethanol. Finally, the NVO powders were obtained by drying at 60 ℃ for 12 h in an oven.

To prepare a cathode for coin-type cell, 60 wt% NVO active materials, 25 wt% Super-P, and 15 wt% polyvinylidene fluoride (PVDF) were thoroughly mixed and dispersed into N-Methyl pyrrolidone (NMP). The resultant slurry was then coated uniformly onto a 14 mm diameter steel mesh, resulting in an ~ 1 mg cm^{-2} active mass loading and a thickness of cathode of ~ 100 μm, followed by drying at 60 ℃ for 12 h.

Preparation of the $Zn_3(OH)_2V_2O_7 \cdot 2H_2O$ powders and cathode

$Zn_3(OH)_2V_2O_7 \cdot 2H_2O$ was prepared by a simple liquid phase precipitation method. 24 mmol $ZnSO_4 \cdot 7H_2O$ was dissolved in 240 mL deionized (DI) water to form a solution, denoted as solution A. 16 mmol NH_4VO_3 was dissolved in 160 mL DI water at 80 °C, denoted as solution B. After that, solution B was added into solution A to form a yellow suspension, and then stirred for 2 h. The pale-yellow precipitates were collected by centrifugation and washed with DI water for 3 times. Finally, the final ZVO product was obtained after drying in vacuum at 60°C for 12 h.

To prepare a cathode for coin-type cell, 60 wt% $Zn_3(OH)_2V_2O_7 \cdot 2H_2O$ active materials, 25 wt% Super-P, and 15 wt% polyvinylidene fluoride (PVDF) were thoroughly mixed and dispersed into N-Methyl pyrrolidone (NMP). The resultant slurry was then coated uniformly onto a 14 mm diameter steel mesh, resulting in an ~ 1 mg cm^{-2} active mass loading and a thickness of cathode of ~ 100 μm, followed by drying at 60 ℃ for 12 h.

Preparation of the polyaniline cathode

In situ deposition of polyaniline (PANI) onto carbon cloth (CC) was performed through a one-step oxidative polymerization process. The carbon cloth was first immersed in 1 M HCl solution (15 mL). Then, 0.365 mL of aniline monomer was added to the above solution. After stirring for 1 h in an ice bath, APS (0.228 g) dissolved in 1 M HCl (5 mL) was added dropwise, and the mixture was further stirred for more than 1 h. The dark green carbon cloth with PANI was sequentially washed with DI water and anhydrous ethanol. Finally, the PANI cathode was obtained by drying at 60 ℃ overnight in an oven, and the mass loading of the PANI on the carbon cloth was approximately 0.6 mg cm^{-2}.

Electrochemical measurements.

In a full ZIB cell, zinc foil with thickness of 100 μm was used as the anode, NVO as the cathode, with hydrogels or glass fiber (Whatman, Grade GF/A) filled with 1 M $ZnSO_4$ aqueous solution (~100 mL) as electrolytes. The battery components were sealed in CR2032-type coin cells using 0.8 ton pressure (cell thickness:2mm). The initial thickness of the as-prepared hydrogel is around 650 μm. Following the application of 0.8 tons of pressure in coin-type cells, the thickness of the hydrogels decreases to approximately 400 μm. Conversely, in pouch cells where no pressure is applied, the thickness of the hydrogel remains at approximately 650 μm.

The ionic conductivities of the hydrogel electrolytes were measured by a Princeton PARSTAT electrochemical workstation. The CR2032-type coin cells and the pouch cells were tested on a LAND battery testing system (CT2001A) at room temperature (293 K). The electrochemical stability of the windows was measured in a three-electrode configuration with a working electrode of Ti foil. The Zn ring and Zn foil were used as the reference electrode and counter electrode, respectively. Chronoamperometric measurements were performed on a Princeton PARSTAT electrochemical working station at an overpotential of -150 mV. A Tafel plot was recorded by a Princeton PARSTAT electrochemical workstation within the voltage range of -0.12 V ~ 0.1 V. Electrochemical impedance spectroscopy (EIS) was performed by a Princeton PARSTAT electrochemical workstation over the frequency range from 100 kHz to 0.1 Hz with a perturbation amplitude of 10 mV.

Materials characterizations.

Fourier transform infrared (FTIR) spectroscopy was performed on a Nicolet 6700 Fourier transform infrared spectroscopy-attenuated total reflection (FTIR-ATR) spectrophotometer. Raman spectra were acquired on a Renishaw microconfocal Raman spectrometer (NanoWizard) with 532 nm excitation. The tensile test was carried out on dumbbell-shaped samples (25 mm × 10 mm × ca. 8 mm) using an Instron 9965 (Norwood, MA) mechanical testing instrument. The contact angles of the water droplets were determined on a drop shape analyser (DSA100), with a volume of 5 μL for each water droplet. The cross-section and surface structures of the hydrogel electrolyte were observed by an environmental scanning electron microscope (ESEM, Quanta650 FEG) under freezing conditions. The morphologies of the Zn anode and the cathode were evaluated by scanning electron microscopy (SEM; FEI Quanta 200 F). The microscopic morphology and elemental mapping were performed via field-emission scanning electron microscopy (FESEM, JSM-7900F) with a Max80 energy dispersive spectrometer (EDS). X-ray diffraction (XRD) was performed on a Rigaku D/MAX-2500/PC instrument with Cu Kα radiation (λ = 1.54 Å) operated at 40 kV and 200 mA. The data were recorded from 5° to 60° with an interval of 0.02° and a scan speed of 5° min^{-1}.

Theoretical calculations.

Density functional theory (DFT) calculations were conducted using the Gaussian 16 software package.[1] All structures were optimized at the B3lyp/6-31+G(d,p) level, followed by normal frequency analyses. All structures were minimized, and no imaginary frequencies were found. Finally, at the B3lyp/6-311+G(d,p) level, the single point energies of all structures are recalculated to get more accurate results. Here, we choose small molecule carbon chain models containing carboxyl and amide groups as the model of PAZPM.

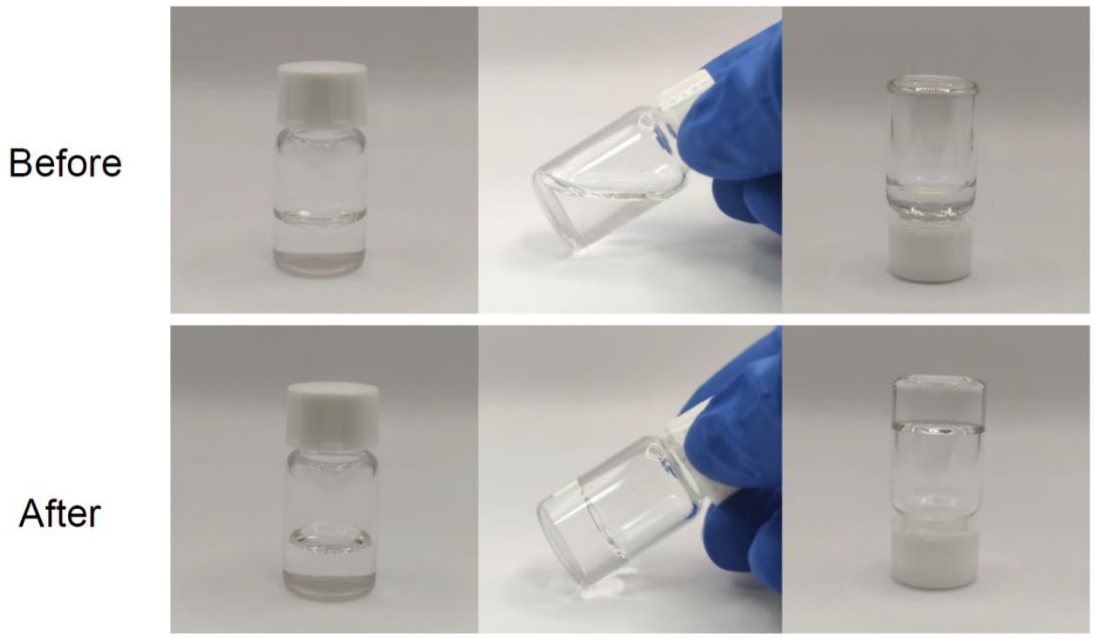

Figure S1. Optical photos of the PAZPM hydrogel before and after polymerization. It should be noted that Zn-AC functions as both a hydrophilic monomer and an ionic crosslinking agent, while MBAA serves as a chemical crosslinking agent. Ammonium persulfate (APS) and N,N,N',N'-tetramethylethylenediamine (TEMED) act as initiator and catalyst, respectively, in copolymerization.

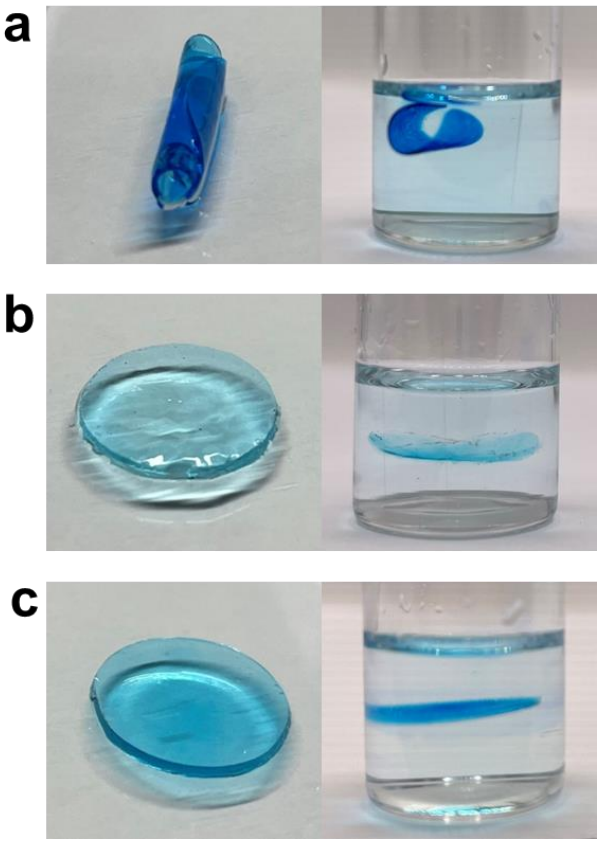

Figure S2. Optical photos of (a) Janus PAZPM, (b) P-PAZPM and (c) G-PAZPM (dyed with methylene blue) in air (left) and in 1 M $ZnSO_4$ aqueous solution (right).

The presence of a greater proportion of hydrophilic monomers at the bottom (glass) side during the copolymerization process led to the formation of a more relaxed polymer chain and an increased pore size. Conversely, the top (PTFE) side exhibited more densely packed polymer chains and an increased presence of hydrophobic groups, resulting in a smaller pore size. The larger pores at the bottom side facilitated greater entrapment of the aqueous solution within the pores, while the smaller pores on the top side allowed less solution retention. In addition to variations in polymer packing density, the gradual divergence in water absorption along the cross section also plays a crucial role in the generation of internal stress. This gradient internal stress becomes the driving force behind the curvature observed in the Janus PAZPM hydrogel, causing it to bend from the more hydrophilic side to the less hydrophilic side (Figure 1a and S2a). As expected, both the symmetrical P-PAZPM and G-PAZPM hydrogels exhibited consistent pore structures throughout the bulk, resulting in flat profiles (Figure 1a, S2b and S2c).

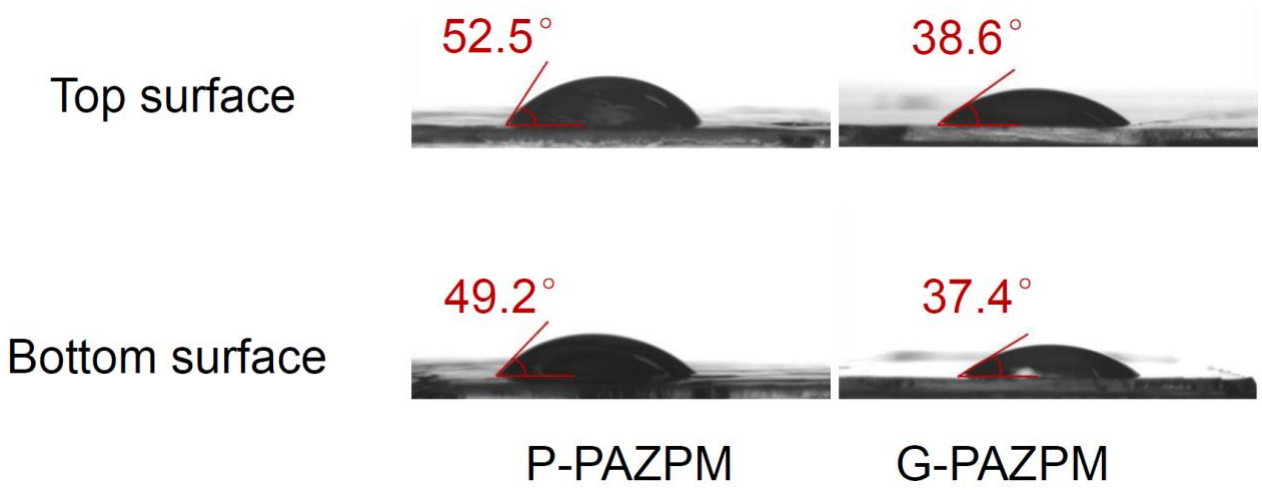

Figure S3. Snapshots recording the contact angles of aqueous $ZnSO_4$ (1 M) electrolyte on the top and bottom surfaces of G-PAZPM and P-PAZPM.

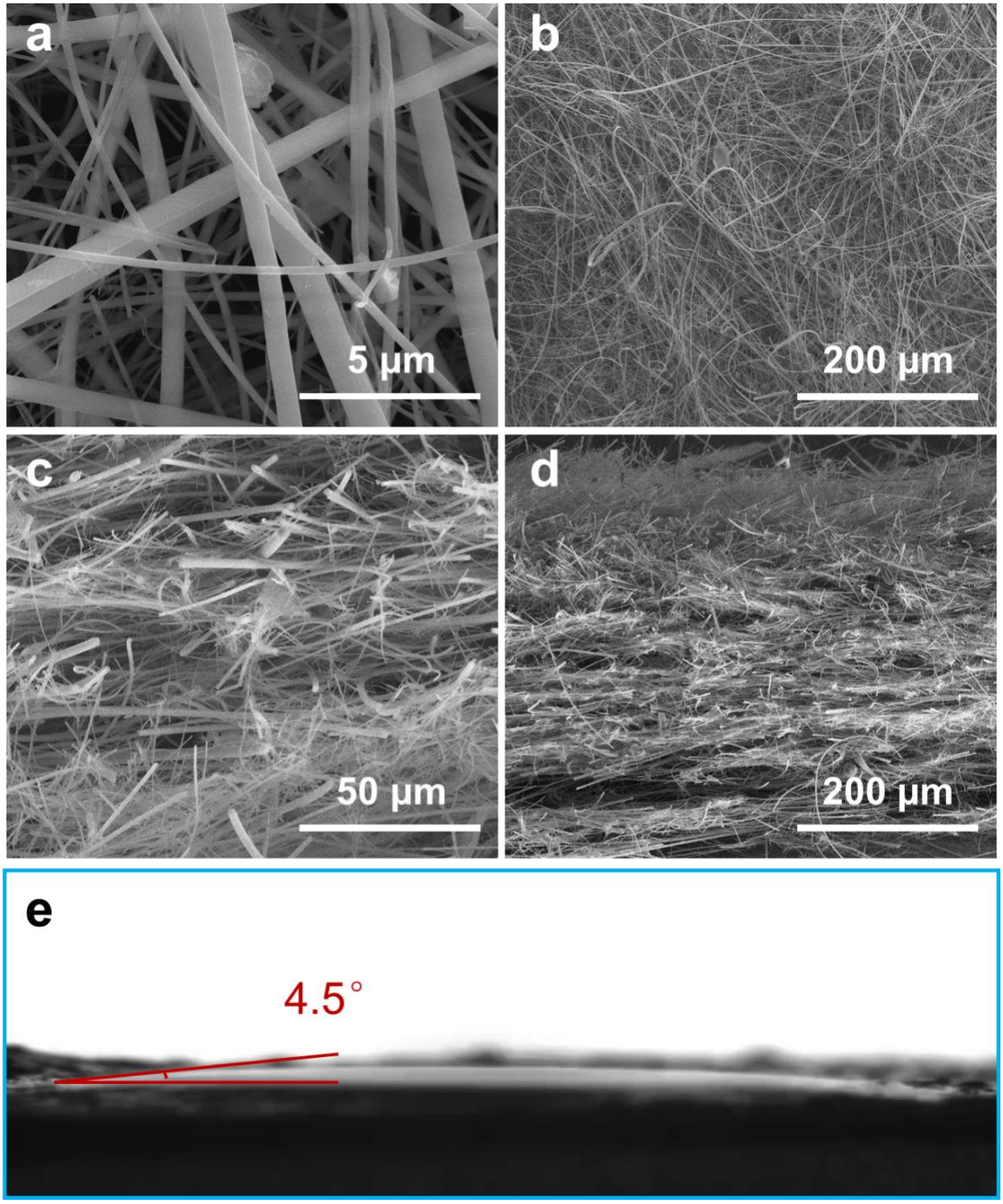

Figure S4. SEM images of the (a, b) surface and (c, d) cross-section of the glass fibre separator at different magnifications. (e) Snapshot recording the contact angles of aqueous $ZnSO_4$ (1 M) electrolyte on the surface of a glass fibre separator.

Notably, the glass fibre separator is superhydrophilic with an observed contact angle of approximately 4.5°. Additionally, video S1 also serves to demonstrate the contact angle.

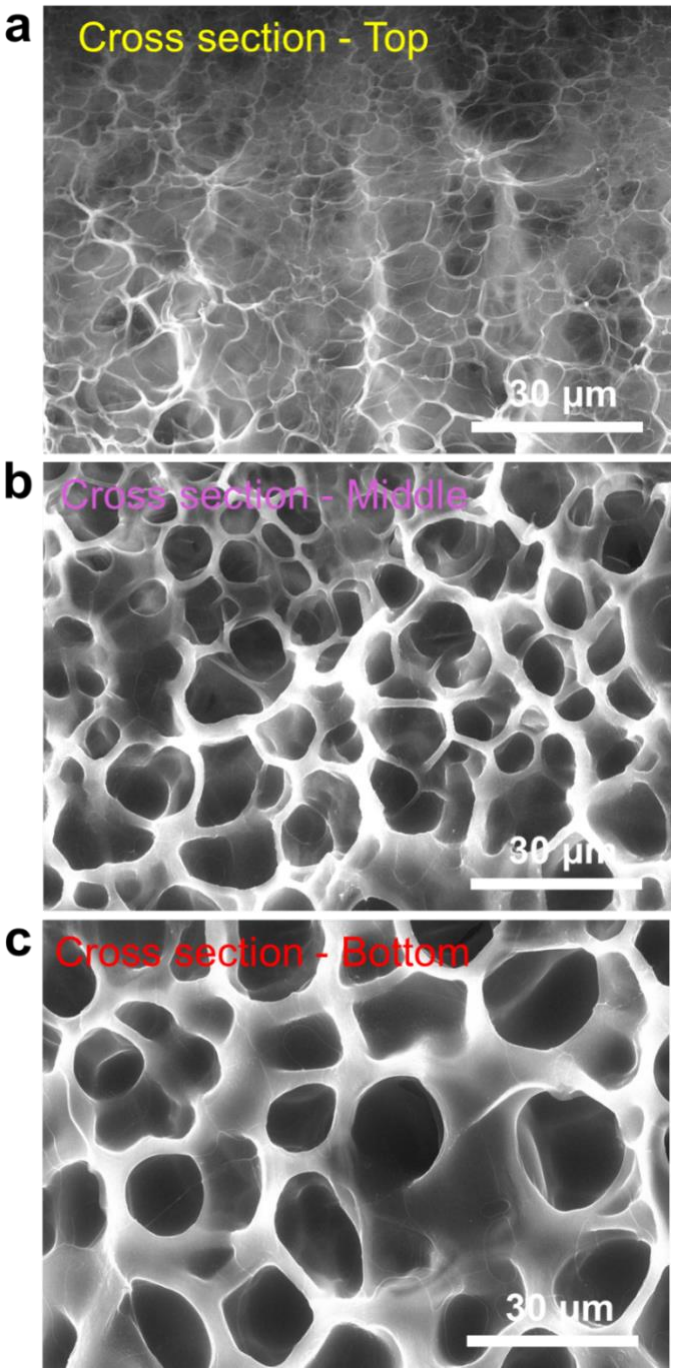

Figure S5. ESEM images of the (a) top, (b) middle and (c) bottom sections of the Janus PAZPM hydrogel.

Clearly, the PAZPM hydrogel exhibited a gradient distribution of pore sizes along the vertical direction of the mold. The gradient pores in the bulk Janus PAZPM hydrogel electrolyte are advantageous for gradient water trapping and Zn^{2+} transport.

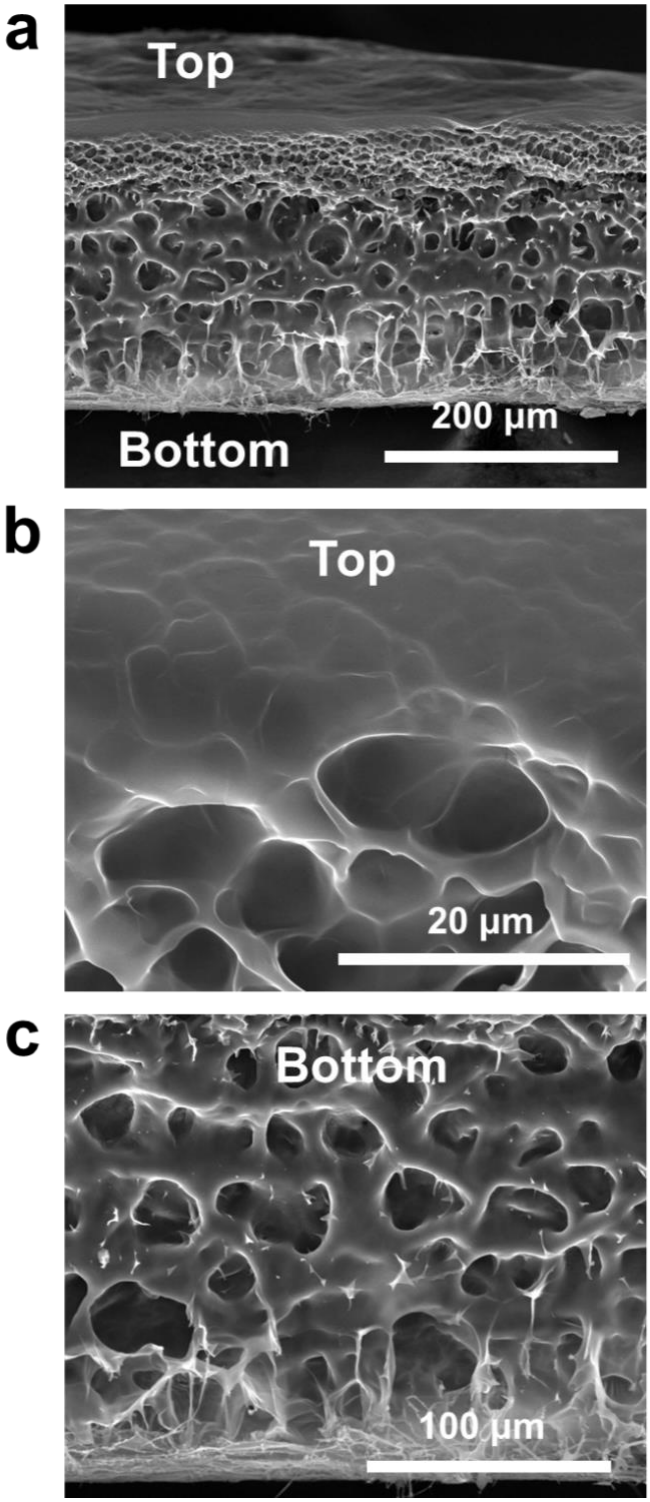

Figure S6. (a) Cross-sectional SEM image of the freeze-dried Janus PAZPM hydrogel. (b, c) Magnified cross-sectional SEM images of the top and bottom sides of the freeze-dried Janus PAZPM hydrogel.

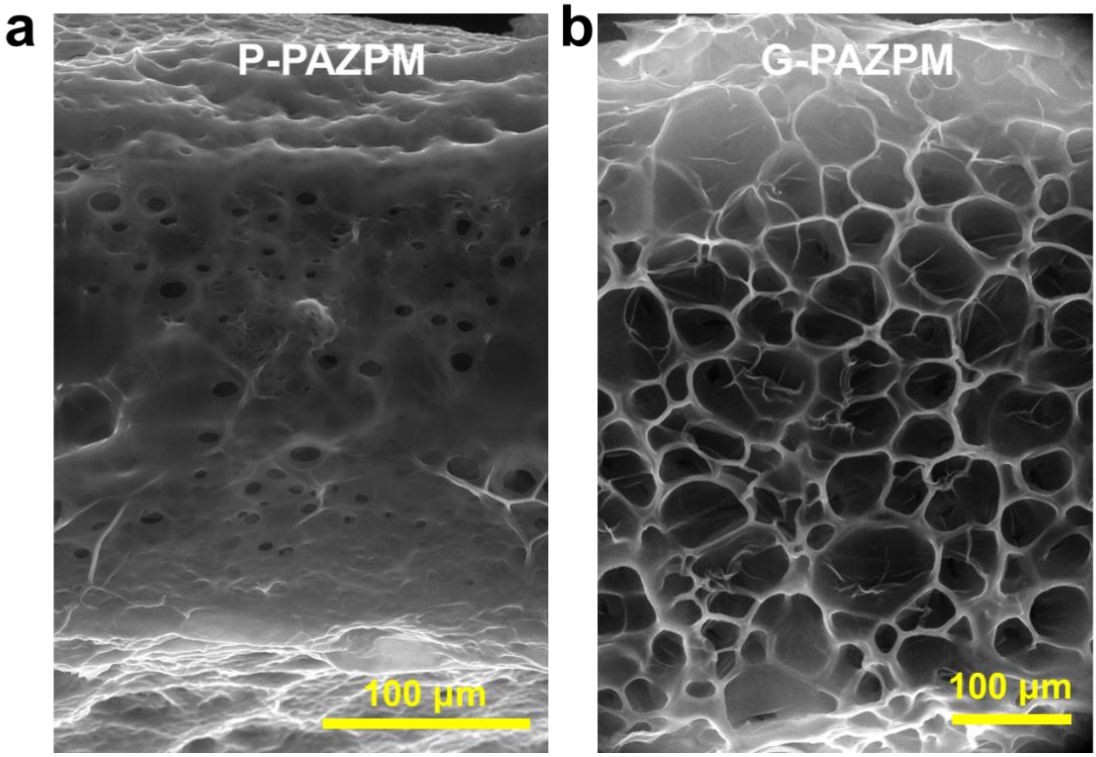

Figure S7. ESEM images of the cross-sections of the (a) symmetrical P-PAZPM and (b) symmetrical G-PAZPM hydrogel electrolytes.

Notably, the symmetrical P-PAZPM electrolytes exhibited greater chain density and denser pores with smaller sizes than did the symmetrical G-PAZPM hydrogel, further underscoring the crucial influence of mold surface polarity on the polymerization process.

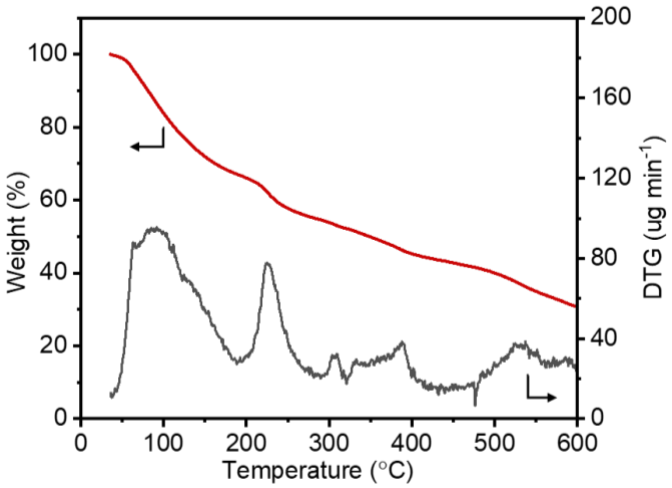

Figure S8. Thermogravimetric analysis of Janus PAZPM hydrogels in N_2 atmosphere at a rate of 10 ℃ min^{-1}.

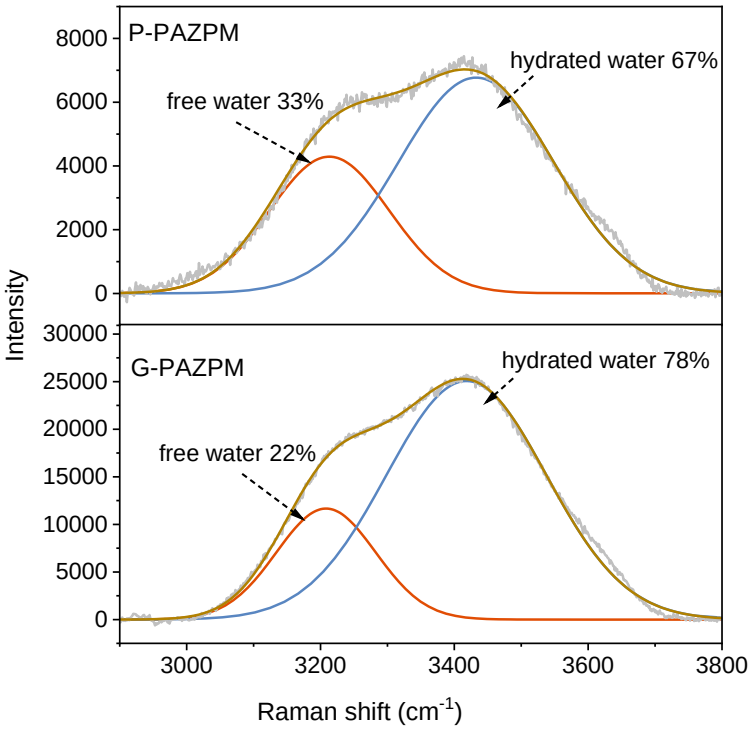

Figure S9 Raman spectra of symmetric P-PAZPM and G-PAZPM.

It's important to highlight that water served as the sole solvent during the hydrogel preparation process. When comparing to the aqueous $ZnSO_4$ electrolyte, differences in water stem from interactions between water molecules and the functional groups within the hydrogels. Variation in the distribution of functional groups in the Janus PAZPM hydrogel leads to differences in the ratios of free water to hydrated water, as well as the total water amount at the same volume (or thickness). To investigate this further, Raman spectroscopy was conducted on symmetric P-PAZPM and G-PAZPM. The aim was to analyze the individual surfaces of the Janus hydrogel separately, thereby mitigating potential interference from the opposite surface. As shown in Figure S9, the water amount of P-PAZPM is notably lower than that of G-PAZPM. Moreover, the ratio of free water to hydrated water in P-PAZPM (33%) is higher compared to that in G-PAZPM (22%). This decrease in the ratio of free water in G-PAZPM can be attributed to interactions between water molecules and hydrophilic groups (such as -COO-, $-CONH_2$, -CONH-).

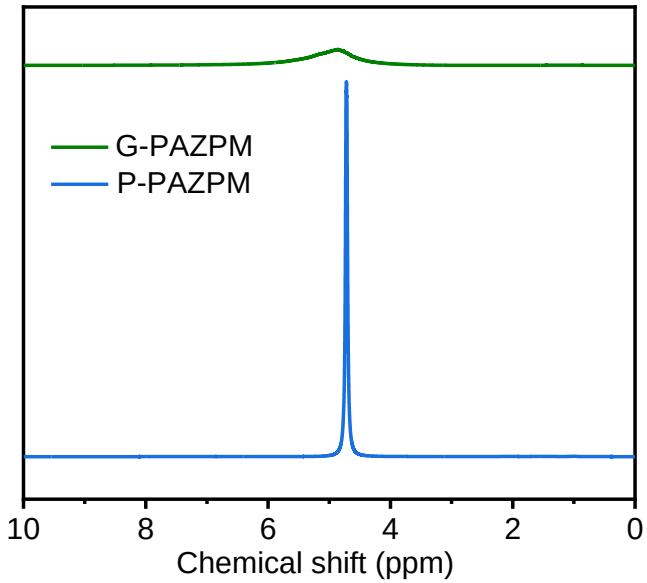

Figure S10 ^{1}H nuclear magnetic resonance (NMR) spectra of symmetric P-PAZPM and G-PAZPM.

In comparison to P-PAZPM, the intensity of the ^{1}H nuclear magnetic resonance (NMR) peak (~4.9 ppm) for G-PAZPM was significantly reduced, while the full width at half maximum (FWHM) for G-PAZPM markedly increased. Additionally, the chemical shift of ^{1}H NMR in G-PAZPM is higher than that in P-PAZPM. These observations further support the formation of strong hydrogen bonds on the more hydrophilic side (glass side) of Janus PAZPM hydrogel due to the robust interactions between water molecules and functional groups. The formation of these strong hydrogen bonds also contributes to the decrease in the ratio of free water to hydrated water on the more hydrophilic side.

By integrating the insights from both Raman and ^{1}H NMR spectra, it becomes evident that the top side (PTFE side) of the Janus hydrogel exhibits reduced hydrophilicity and lower water amount compared to the bottom side (glass side). This phenomenon arises from the dense stack of hydrophobic polymer main chains and hydrophobic groups (such as isopropyl) on the top side. In contrast, the bottom side (glass side) demonstrates higher hydrophilicity owing to the presence of hydrophilic groups on the polymer main chains. This higher hydrophilicity facilitates strong interactions between the hydrophilic groups and the aqueous $ZnSO_4$ electrolytes, thereby greatly enhancing hydrogen bonding and influencing water activity.

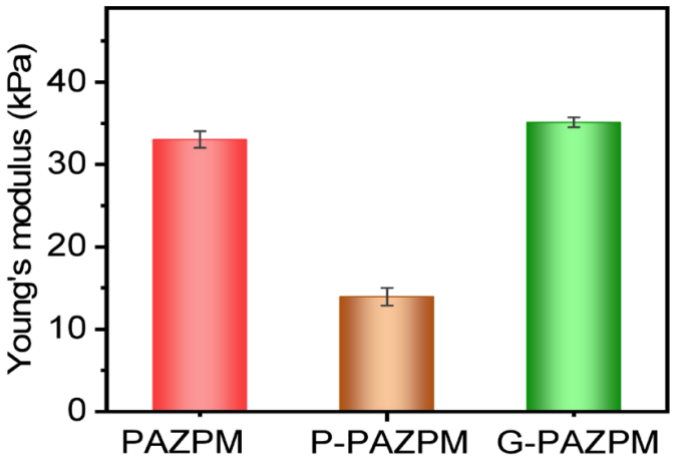

Figure S11. Young's modulus of the Janus PAZPM, symmetrical P-PAZPM and symmetrical G-PAZPM hydrogels.

While the extension ratio of the Janus PAZPM hydrogel was slightly lower than that of P-PAZPM, it surpassed that of G-PAZPM. Additionally, the Young's modulus of the Janus PAZPM hydrogel was only marginally lower than that of G-PAZPM but was significantly greater than that of P-PAZPM. This occurs because the increased aggregation of hydrophobic segments leads to a decrease in the number of hydrogen bonds between the hydrophilic amide groups and water molecules, primarily due to the lack of hydrophilic groups. Consequently, a decrease in the number of hydrogen bonds results in a lower Young's modulus. Nevertheless, the presence of denser polymer chains, with fewer restricted segments affected by hydrogen bonds, contributes to an enhancement in the elongation properties of the hydrogel.

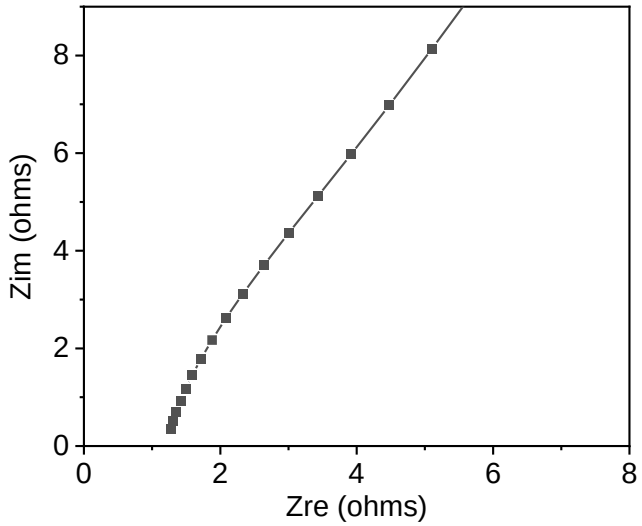

Figure S12. Nyquist plots of the electrolyte using glass fibre (thickness: 400 μm) filled with 1 M $ZnSO_4$ aqueous solution.

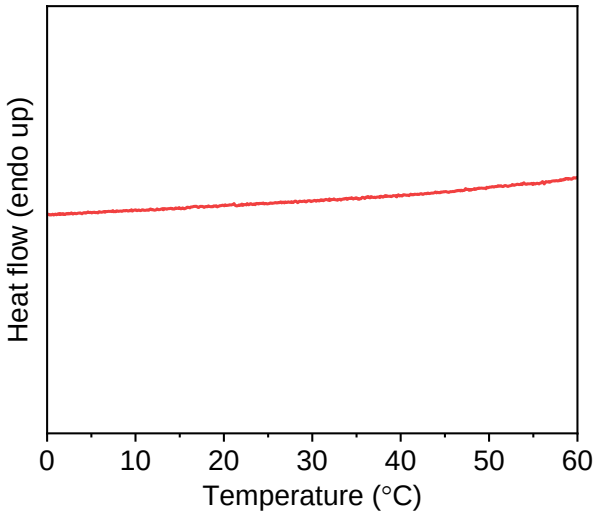

Figure S13. Differential scanning calorimetry (DSC) curves of Janus PAZPM hydrogel.

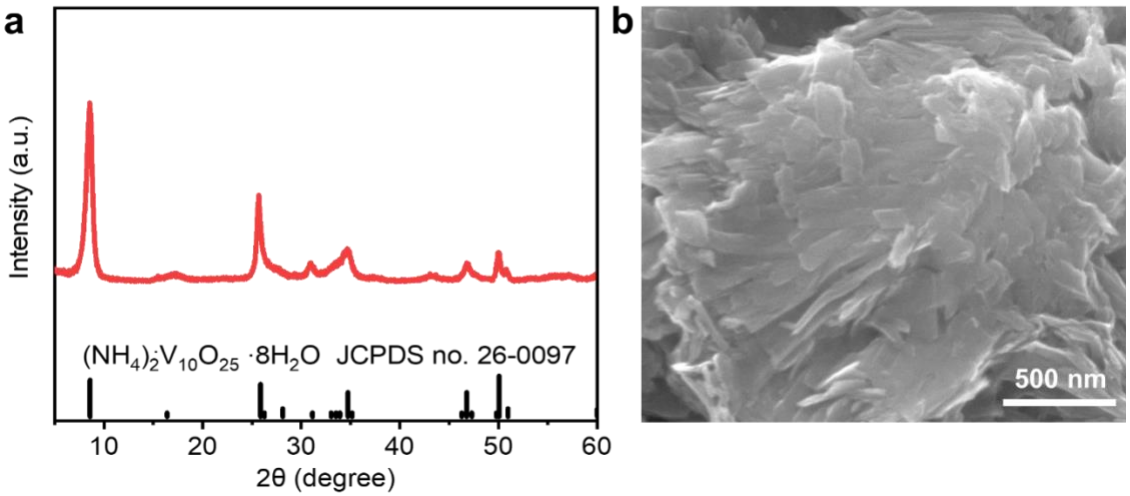

Figure S14. (a) XRD pattern and (b) SEM image of the as-prepared $(NH_4)_2V_{10}O_{25}\cdot 8H_2O$ (NVO) powders.

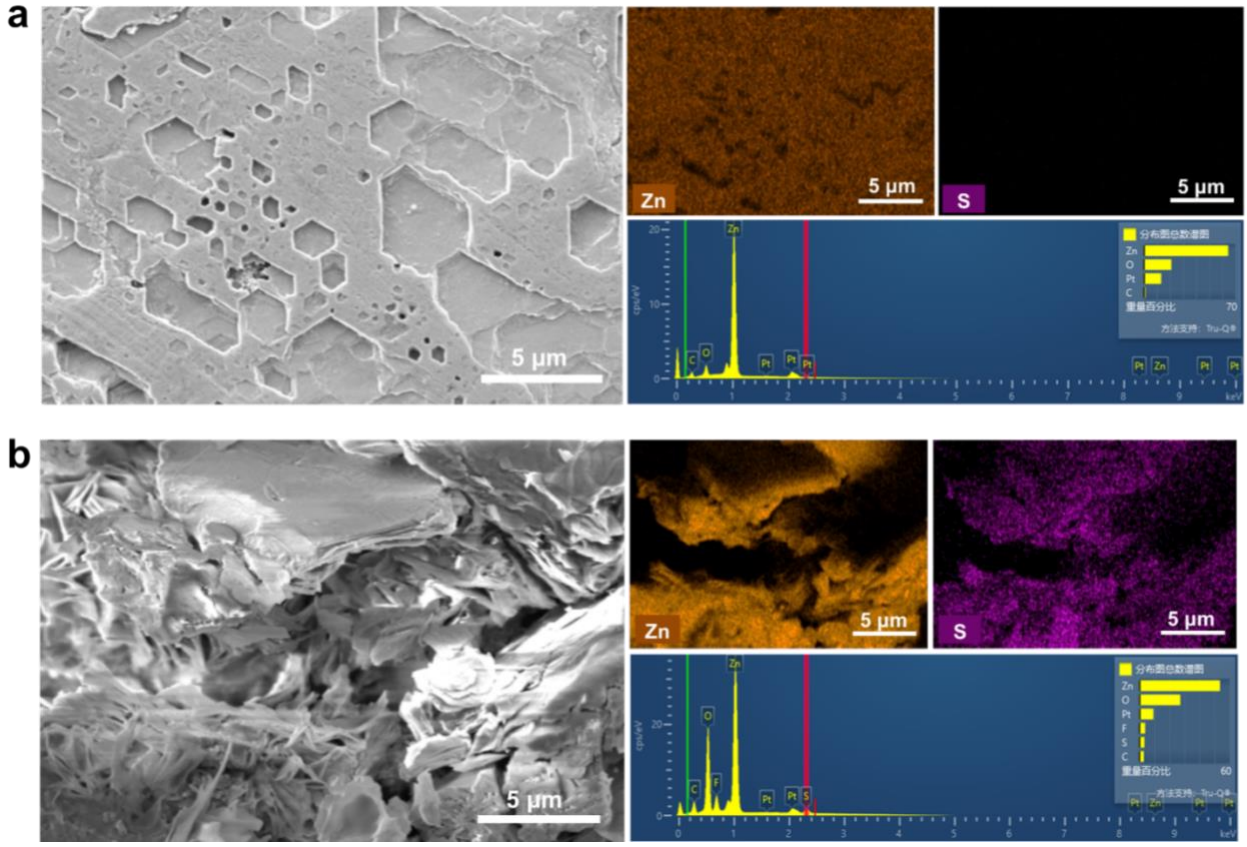

Figure S15. Elemental distribution analysis of the cycled Zn anode using (a) the Janus PAZPM hydrogel and (b) the GF separator (1 M $ZnSO_4$) after 100 cycles at 0.5 A g^{-1}.

In contrast to the cycled Zn anode using the Janus PAZPM hydrogel electrolyte, the Zn anode subjected to cycling with a GF separator filled with 1 M $ZnSO_4$ aqueous solution exhibited the presence of S, directly demonstrating the formation of $Zn_4(OH)_6SO_4 \cdot 4H_2O$ (ZSH) byproducts. Additionally, the Zn deposits obtained with the Janus PAZPM hydrogel electrolyte displayed a more uniform and orderly arrangement than those observed with GF.

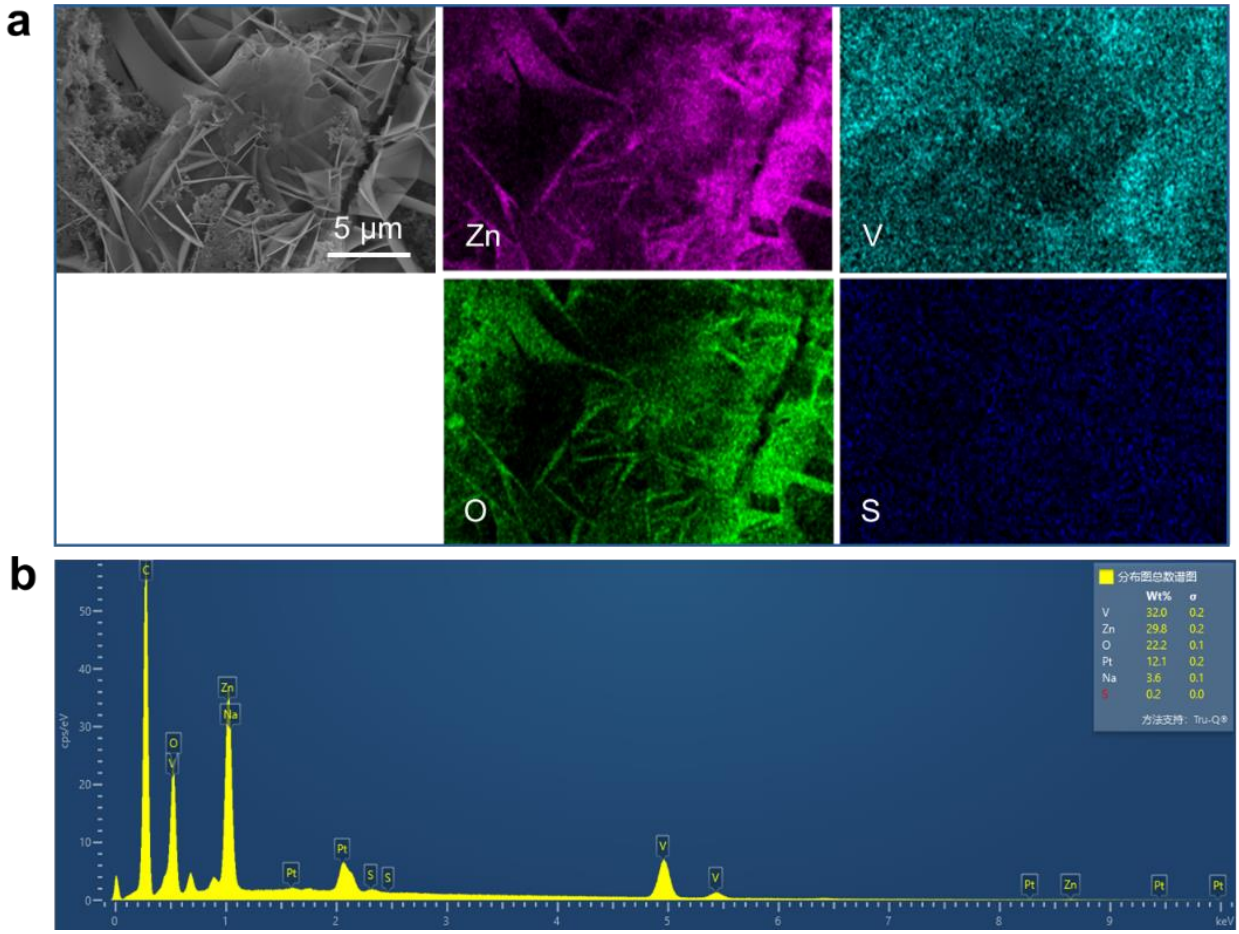

Figure S16 (a) SEM image and corresponding element mappings, and (b) energy-dispersive spectroscopy (EDS) analysis of NVO cathode after 100 cycles at 0.5 A g^{-1} using glass fiber filled with 1 M $ZnSO_4$.

Besides the distinct XRD peaks signifying $Zn_3(OH)_2V_2O_7{\cdot}2H_2O$ (as displayed in Figure 2f), the energy-dispersive spectroscopy (EDS) mapping presented in Figure S16 clearly indicates that the nanoflakes observed on the surface of cycled NVO cathodes are primarily composed of Zn, V and O, with no presence of S. It's noteworthy that the presence of Pt results from sputtering deposition onto the sample surface, aimed at improving electronic conductivity to achieve higher-quality SEM images.

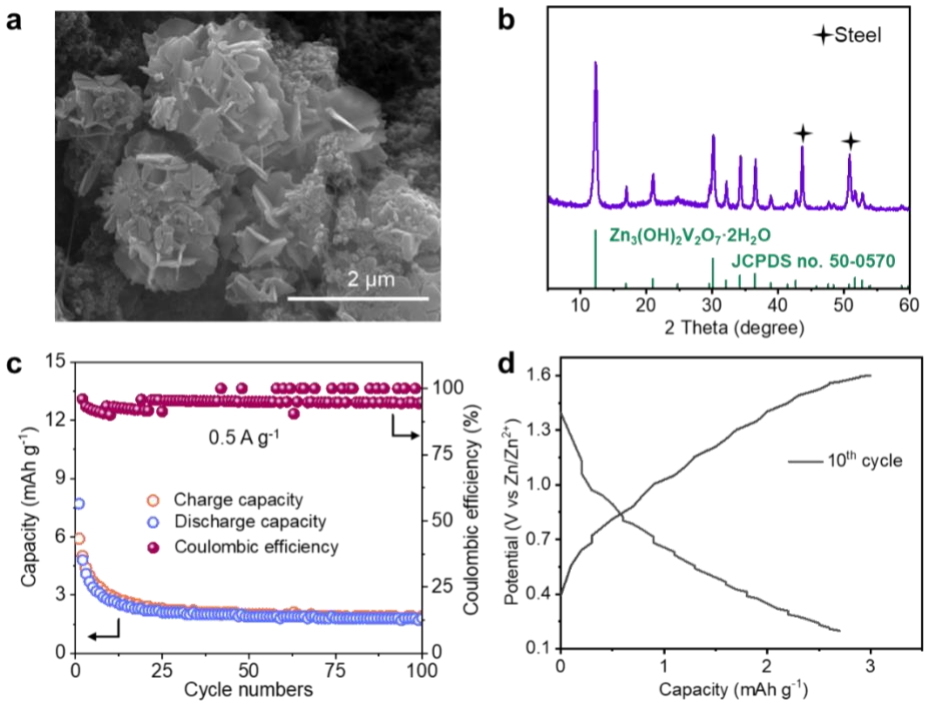

Figure S17 (a) SEM image and (b) XRD pattern of $Zn_3(OH)_2V_2O_7{\cdot}2H_2O$ cathode. (c) Cycling performance at 0.5 A g^{-1}, and (d) charge/discharge curves at the 10^{th} cycle of the Zn|| $Zn_3(OH)_2V_2O_7{\cdot}2H_2O$ in GF filled with $ZnSO_4$ aqueous electrolyte.

$Zn_3(OH)_2V_2O_7{\cdot}2H_2O$ was directly synthesized, as illustrated in Figure S17a and S17b. However, Figure S17c and S17d demonstrate that $Zn_3(OH)_2V_2O_7{\cdot}2H_2O$ exhibits minimal activity, yielding only around 3.5 mAh g^{-1}. Hence, the formation of $Zn_3(OH)_2V_2O_7{\cdot}2H_2O$ appears to have a detrimental effect on cycling stability.

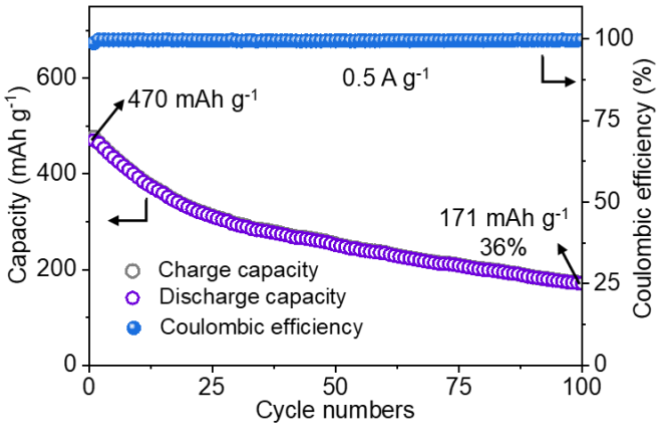

Figure S18 The cycling performance at 0.5 A g^{-1} of the Zn||NVO full cells using the reverse Janus PAZPM configuration, wherein the more hydrophilic side (bottom side) of the Janus PAZPM hydrogel is oriented toward the Zn anode while the less hydrophilic side (top side) faces the cathode.

Optimizing the hydrophilicity of both sides of the Janus hydrogels

To adjust the hydrophilicity on both sides of the Janus hydrogels, the proportion of the hydrophobic monomer NIPAM was systematically varied from 0% to 25% (molar ratio), as outlined in Table S1. The resulting Janus PAZPM hydrogel electrolyte was denoted as X-PAZPM, where X represents the molar ratio of NIPAM to the initial raw material. Upon introducing NIPAM, the difference in the FT-IR spectra of the two sides becomes obvious (Figure S19), indicating enrichment of different functional groups on the two sides. Additionally, an increase in the NIPAM content resulted in an increase in the contact angle (i.e., a decrease in hydrophilicity) on both sides of the PAZPM hydrogel (Figure S20) while preserving the Janus characteristics. Moreover, the ionic conductivity decreases from 24.2 mS cm^{-1} to 10.8 mS cm^{-1} with increasing NIPAM proportion (Figure S21).

Figure S22 shows the performance of Zn||NVO full cells prepared using Janus hydrogel electrolytes with various amounts of hydrophobic NIPAM monomers. As the NIPAM content increased from 0 to 15%, the capacity retention of the Zn||NVO full cells improved from 53% to 87% after 100 cycles at 0.5 A g^{-1}. However, further increases in the NIPAM content from 15 to 25% resulted in a decrease in the cycling stability. Notably, all the Zn||NVO cells prepared using Janus PAZPM hydrogel electrolytes exhibited greater capacity retention than did those prepared using an aqueous electrolyte with GF (only 25% after 100 cycles), highlighting the advantages of Janus hydrogel electrolytes.

As the surface hydrophilicity (i.e., water activity) decreased, there was a noticeable inhibitory effect on the formation of zinc sulfate hydroxide (ZSH) as a byproduct on the cycled Zn anode (Figure S23 and S24), while there was a trend toward the generation of $Zn_3(OH)_2V_2O_7{\cdot}2H_2O$ byproducts on the cathode side (Figure S25 and S26). In brief, the less hydrophilic side of the Janus PAZPM hydrogel electrolyte exhibited dense and compact pores of small sizes, contributing to the decrease in water molecule activity on the surface of the Zn anode. This characteristic serves as a positive feedback mechanism, aiding in the inhibition of water-induced corrosion. Additionally, the functional groups present on the hydrophobic surface of the PAZPM hydrogel electrolyte play a beneficial role in promoting the steady, uniform and parallel deposition of Zn. Notably, however, an excessively strong hydrophobic character may lead to the formation of $Zn_3(OH)_2V_2O_7{\cdot}2H_2O$ byproducts on the cathode. These findings further underscore the importance of an optimal hydrophilicity (water activity) for ensuring the stability of both anodes and cathodes. Due to its exceptional cycling performance, further investigations were conducted on the Janus PAZPM hydrogel electrolyte containing 15% NIPAM. It is essential to emphasize that the Janus PAZPM hydrogel was prepared using 15% NIPAM; therefore, Janus PAZPM is equivalent to the 15%-PAZPM hydrogel.

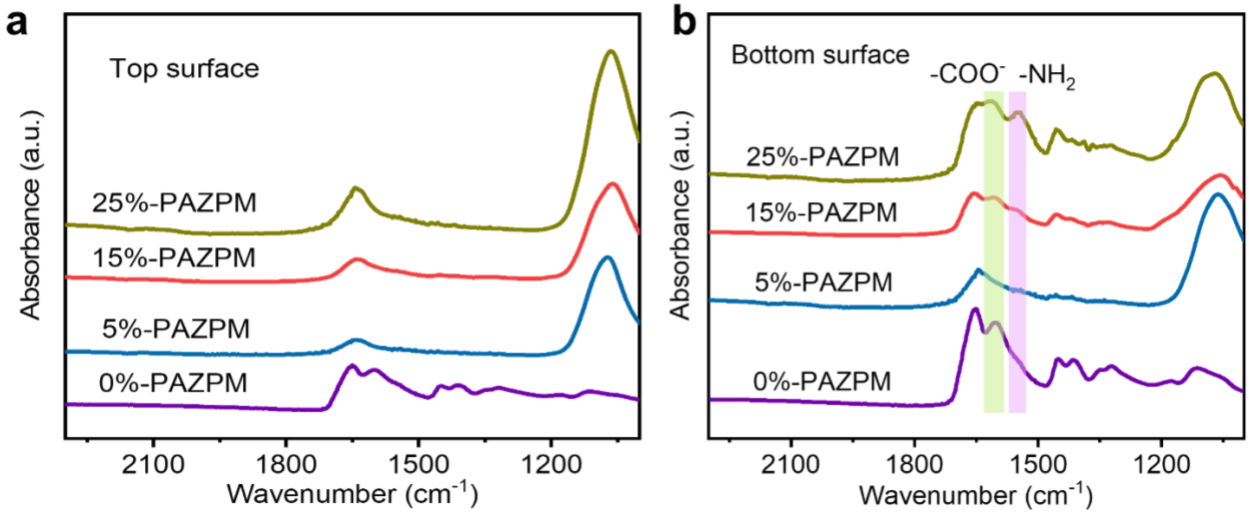

Figure S19. FTIR spectra of the (a) top surfaces and (b) bottom surfaces of the Janus PAZPM hydrogels with various amounts of NIPAM. The sample labelled 15%-PAZPM is identical to the one designated PAZPM.

The Janus 0%-PAZPM hydrogel shows similar FT-IR spectra, featuring distinct peaks corresponding to hydrophilic groups on both sides, albeit with slight intensity variations attributed to the absence of hydrophobic groups.

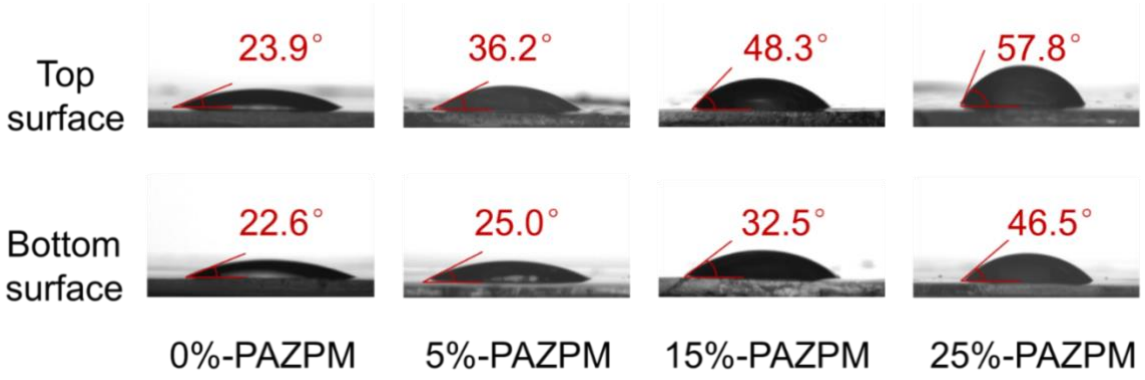

Figure S20. Snapshots recording the contact angles of aqueous $ZnSO_4$ (1 M) electrolyte on the surfaces of Janus PAZPM hydrogel electrolytes with various amounts of NIPAM. The contact angle of the less hydrophilic side of the Janus PAZPM hydrogels increased (from 23.9° to 57.8°) as the content of NIPAM increased from 0% to 25%. Additionally, the contact angles on the more hydrophilic sides were lower than those on the less hydrophilic sides of the Janus PAZPM hydrogel.

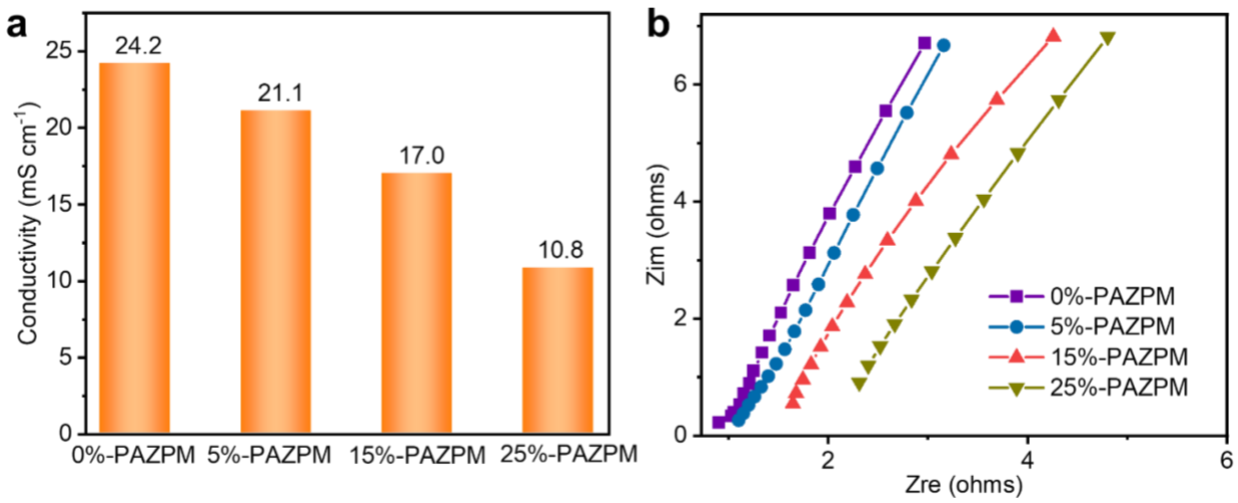

Figure S21. (a) Ionic conductivities and (b) Nyquist plots of Janus PAZPM hydrogel electrolytes with various amounts of NIPAM.

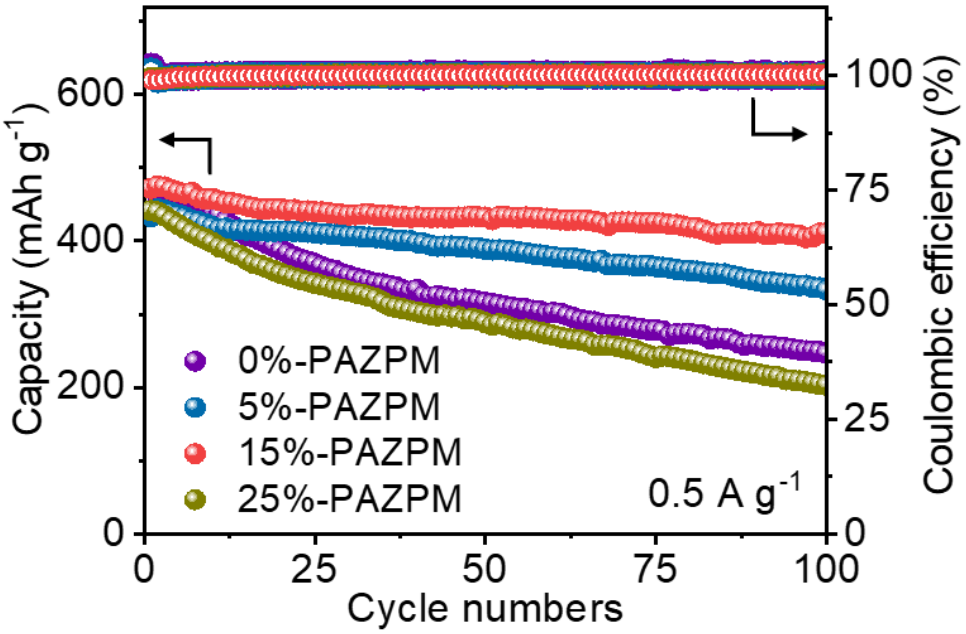

Figure S22. Cycling performance of the Zn||NVO full cells obtained at 0.5 A g^{-1} using Janus PAZPM hydrogel electrolytes with various amounts of hydrophobic NIPAM. The sample labelled 15%-PAZPM is identical to the one designated PAZPM.

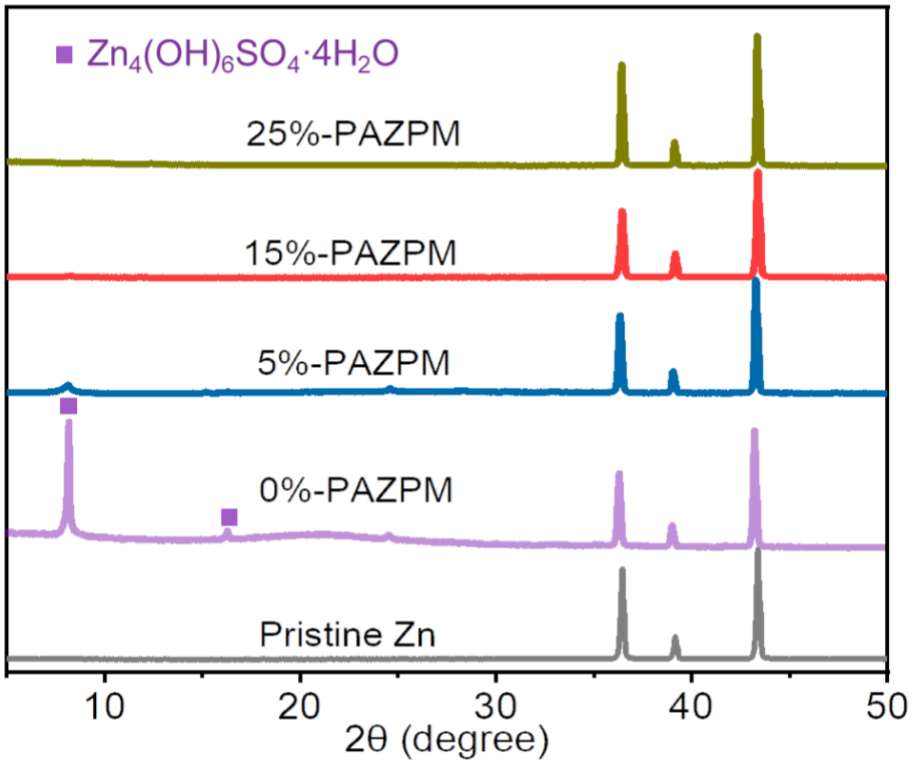

Figure S23. XRD patterns of the cycled Zn anodes after 100 cycles at 0.5 A g^{-1} using PAZPM hydrogel electrolytes with various amounts of hydrophobic NIPAM. The sample labelled 15%-PAZPM is identical to the one designated PAZPM.

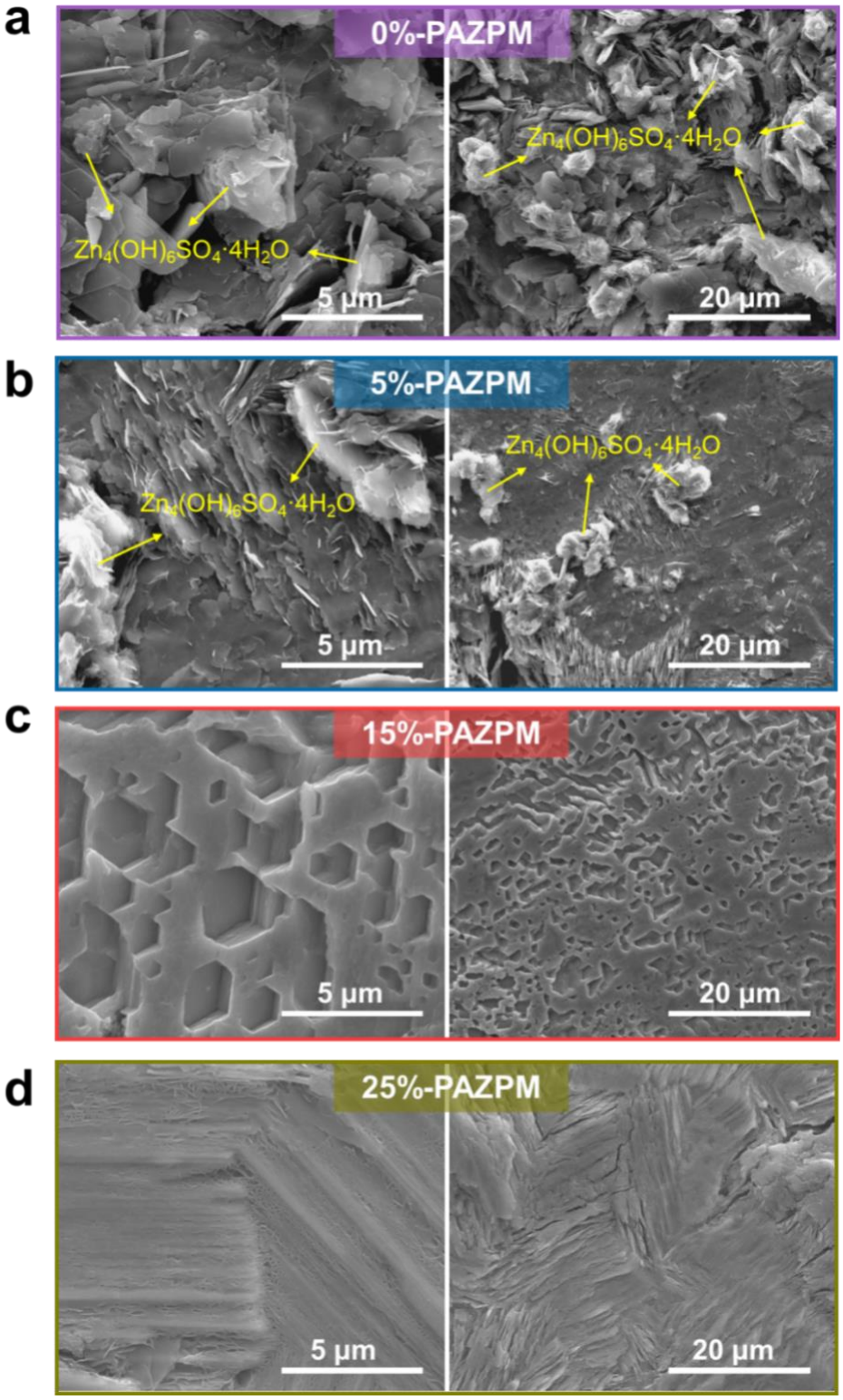

Figure S24. SEM images of the cycled Zn anodes after 100 cycles at 0.5 A g^{-1} with (a) 0%-PAZPM, (b) 5%-PAZPM, (c) 15%-PAZPM and (d) 25%-PAZPM hydrogel electrolytes. The sample labelled 15%-PAZPM is identical to the one designated PAZPM.

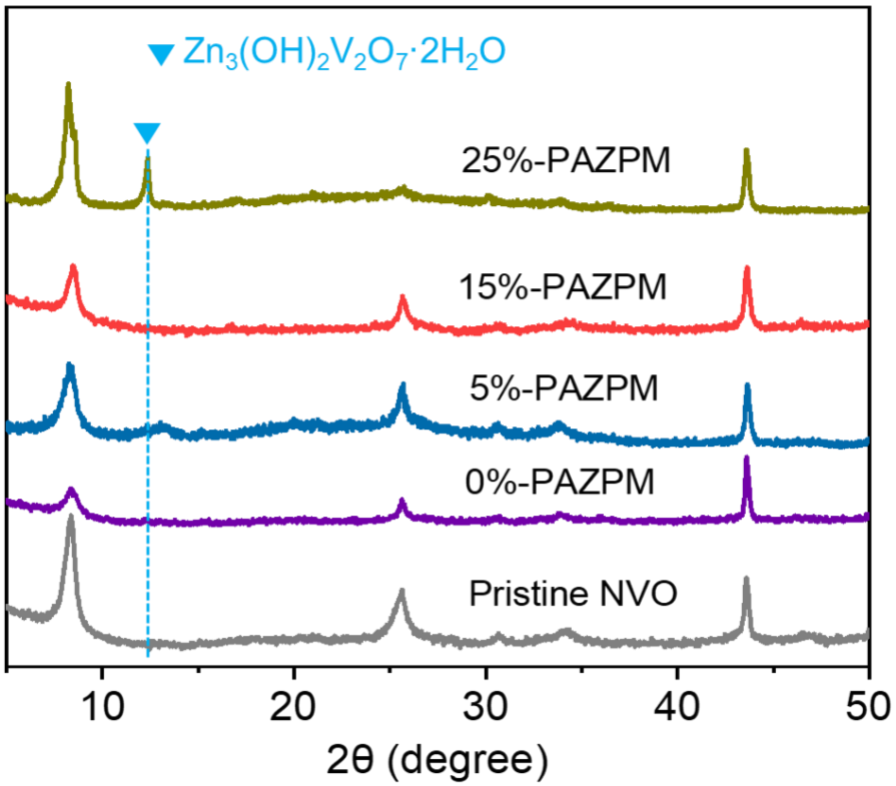

Figure S25. XRD patterns of the cycled NVO cathodes prepared using PAZPM hydrogel electrolytes with various amounts of hydrophobic NIPAM after 100 cycles at 0.5 A g^{-1}.

Notably, $Zn_3(OH)_2V_2O_7 \cdot 2H_2O$ exhibits no activity in aqueous zinc-ion batteries (Figure S17), thereby acting as an undesirable byproduct.[2]

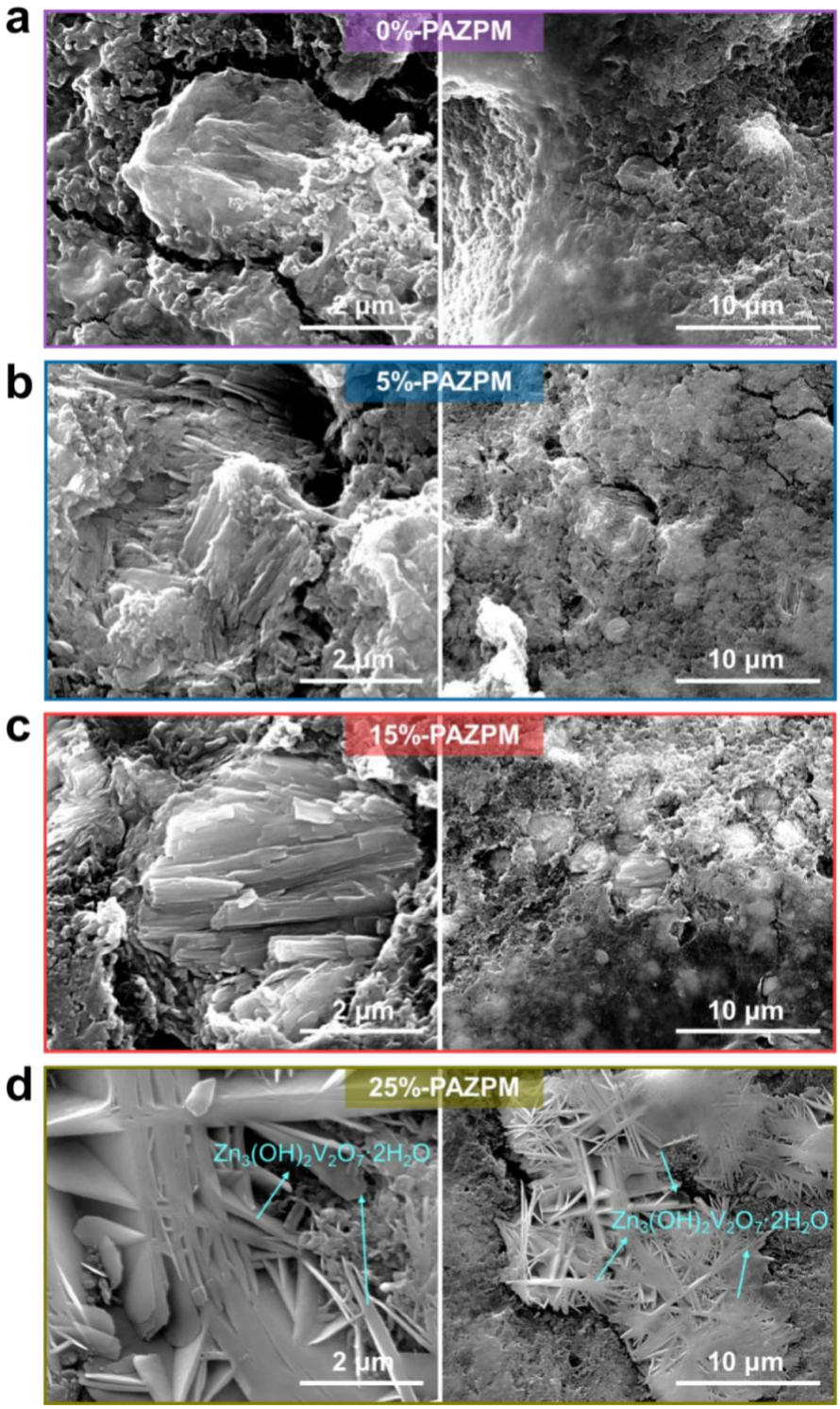

Figure S26. SEM images of the cycled NVO cathodes after 100 cycles at 0.5 A g^{-1} with (a) 0%-PAZPM, (b) 5%-PAZPM, (c) 15%-PAZPM and (d) 25%-PAZPM hydrogel electrolytes.

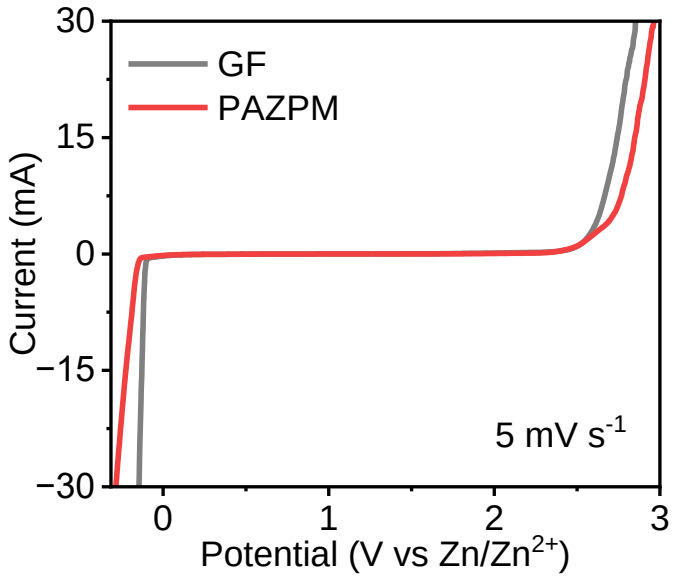

Figure S27. The electrochemical stability windows of Janus PAZPM hydrogel electrolytes and 1 M $ZnSO_4$ electrolyte (using GF) (working electrode: Ti foil; counter electrode: Zn foil; reference electrode: Zn ring).

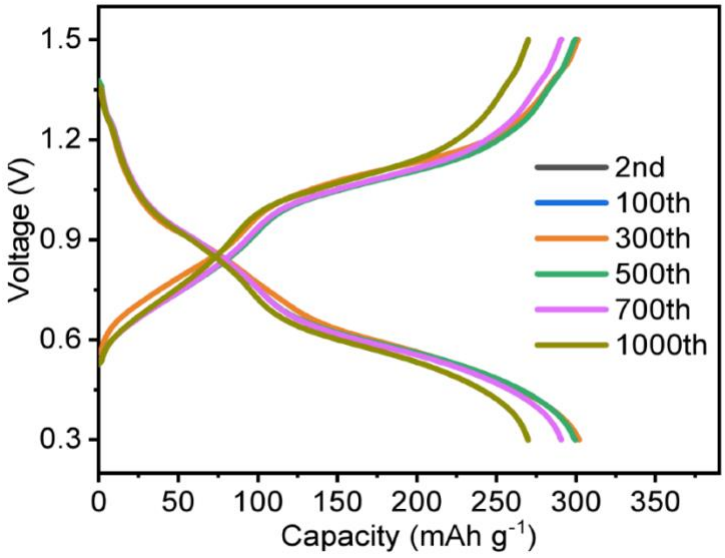

Figure S28. Galvanostatic charge/discharge profiles at certain cycles of the Zn||NVO full cell using the PAZPM hydrogel electrolytes at 5 A g^{-1}.

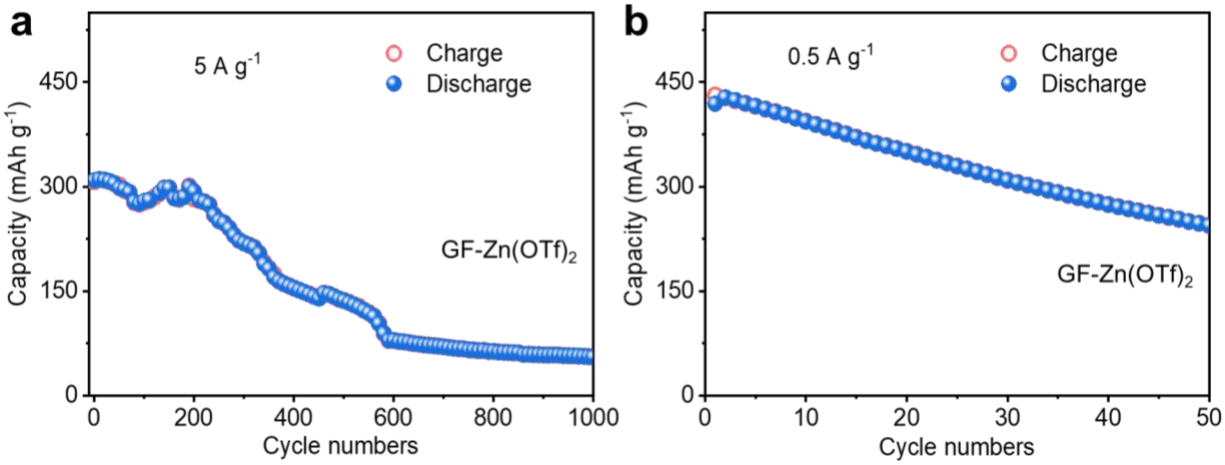

Figure S29. Cycling performances at (a) 5 A g^{-1} and (b) 0.5 A g^{-1} of the Zn||NVO full cell using the GF separator filled with 1 M $Zn(OTf)_2$ aqueous electrolyte (GF-$Zn(OTf)_2$).

Additionally, at a low current density of 0.5 A g^{-1}, Zn||NVO utilizing a 1 M $Zn(OTf)_2$ aqueous electrolyte with a GF separator exhibited far lower cycling stability than that achieved using Janus PAZPM (Figure 2b and S29b).

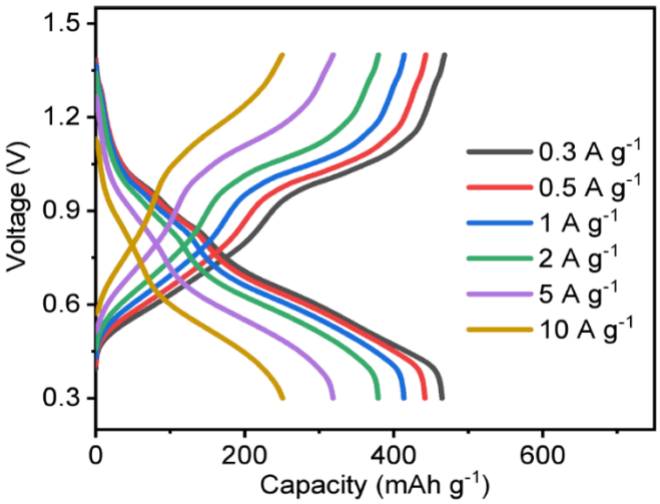

Figure S30. Galvanostatic charge/discharge profiles of the Zn||NVO full cell using the Janus PAZPM hydrogel electrolyte at various rates.

Impressively, as the current density ranged from 0.3 to 10 A g^{-1}, the capacity of the Janus PAZPM hydrogel surpassed that of the $ZnSO_4$ aqueous electrolyte with a GF separator (Figure 2h), demonstrating the superior rate capability of the Janus PAZPM hydrogel.

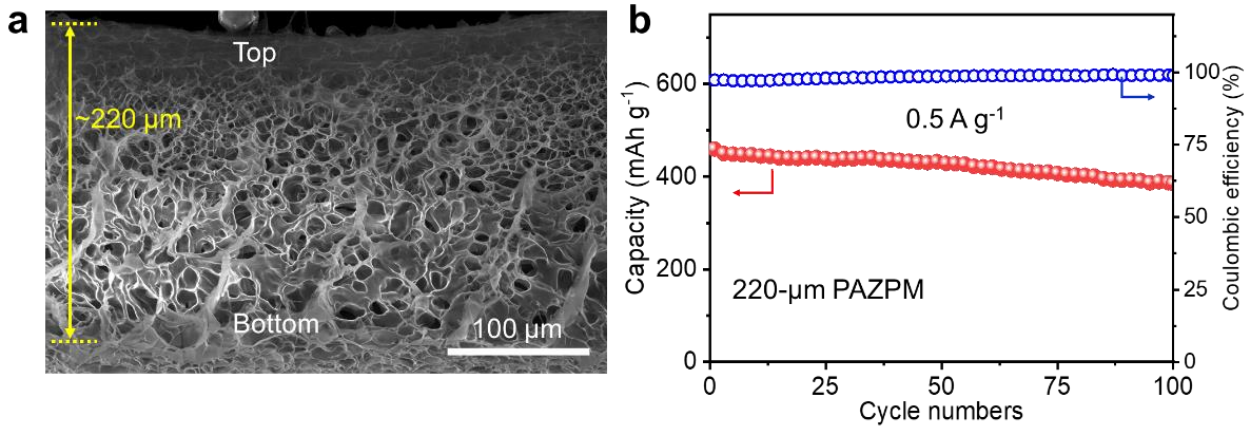

Figure S31 (a) Cross-sectional view of the Janus PAZPM hydrogel electrolyte. (b) Cycling performance of the Zn||NVO full cell with the thin Janus PAZPM hydrogel electrolyte (thickness: ~220 μm).

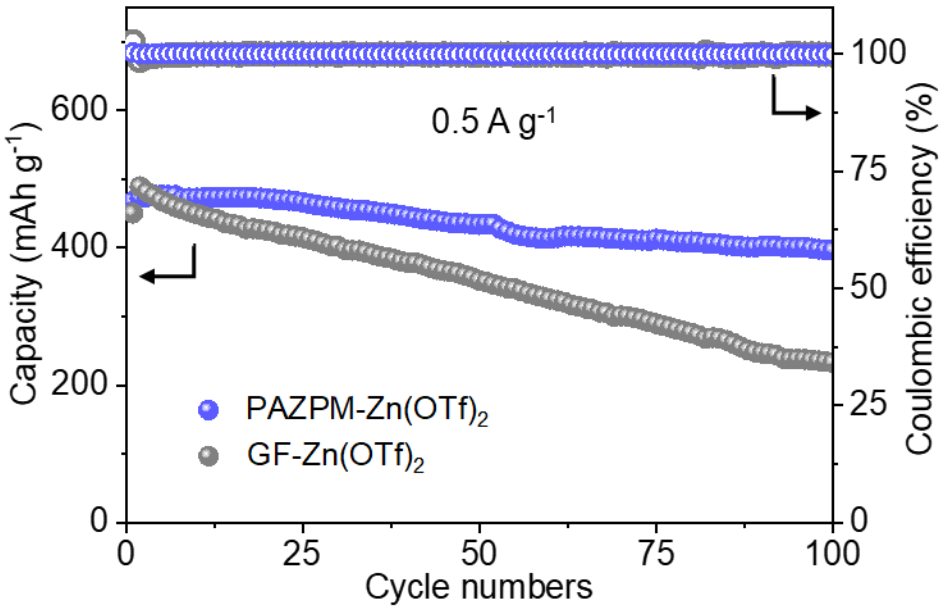

Figure S32. The cycling performances at 0.5 A g^{-1} of the Zn||NVO full cells using the Janus PAZPM with 1M $Zn(OTf)_2$ and GF filled with 1M $Zn(OTf)_2$.

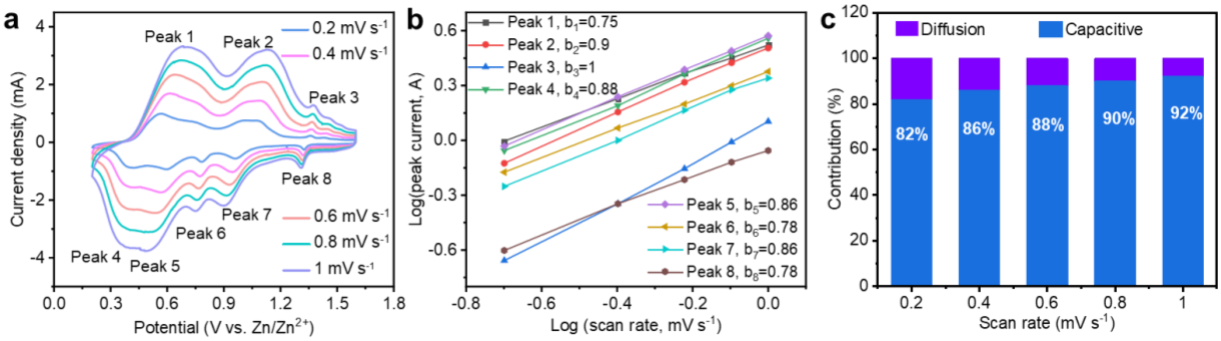

Figure S33 (a) CV profiles of Zn||NVO cell using Janus PAZPM hydrogel electrolyte at various scan rates. (b) Plots of log (peak current) vs log (scan rate). (c) The capacity and diffusion contribution ratios at different scan rates.

To understand the kinetic behavior, CV measurements were carried out at different scan rates from 0.2 to 1.0 mV s^{-1} (Figure S33a). Generally speaking, the peak current (i) of CVs can be related to scan rate by an empirical power-law relationship, which can be expressed as a combination of surface-controlled capacitive effects ($i_1=k_1v$) and diffusion-controlled Zn^{2+} (de)intercalation process ($i_2=k_2v^{1/2}$):

$$i = k_1v+k_2v^{1/2}\approx av^b \quad (1)$$

where k_1, k_2, a and b are variable parameters; b=0.5 for a diffusion-controlled charge-transfer process and 1.0 for a surface-controlled capacitive process.

Figure S33b shows b-values obtained from the slopes of log(current) *vs* log (scan rate), *i.e.* 0.75, 0.9, 1, 0.88, 0.86, 0.78, 0.86, 0.78 for the redox peaks observed in Figure S33a, respectively. The level of the b-value implies that both the surface-controlled capacitive and diffusion-limited redox processes are involved in the charge storage process. Furthermore, the ratio of relative capacitive and diffusional contribution to the total capacity suggests that there is 82% capacitive contribution at a scan rate of 0.2 mV s^{-1} (see Figure S33c), with the scan rate increasing from 0.2 to 1.0 mV s^{-1}, the ratio of capacitive contribution increases from 82 to 92%.

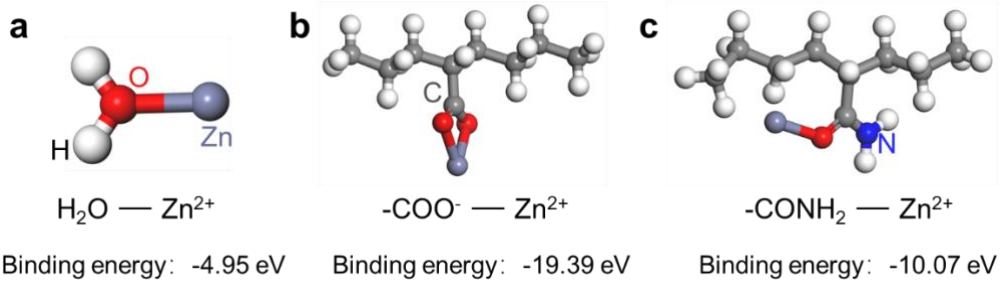

Figure S34. The structures and binding energies of interactions between Zn^{2+} and H_2O/functional groups (including carboxyl and amide groups) on the polymer chains.

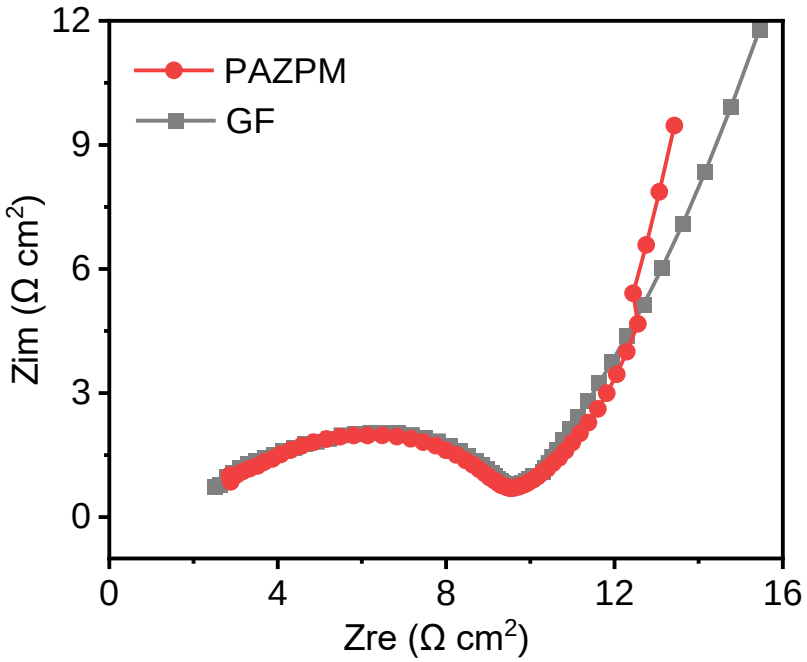

Figure S35. EIS spectra at the open circuit voltage (OCV) state for NVO cathodes using three electrode cells (working electrode: NVO cathode; reference electrode: Zn ring; counter electrode: Zn foil).

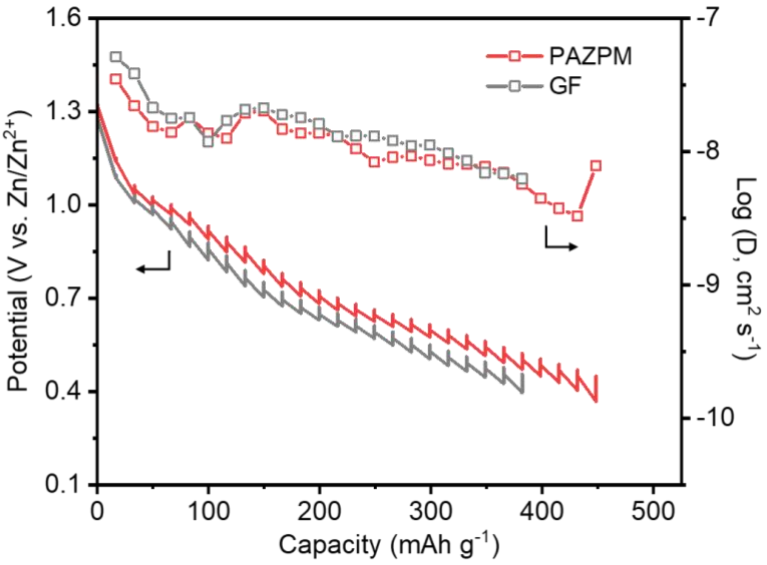

Figure S36. The ionic diffusion coefficients of NVO cathodes using the Janus PAZPM hydrogel electrolyte and a GF separator filled with 1 M $ZnSO_4$ aqueous solution.

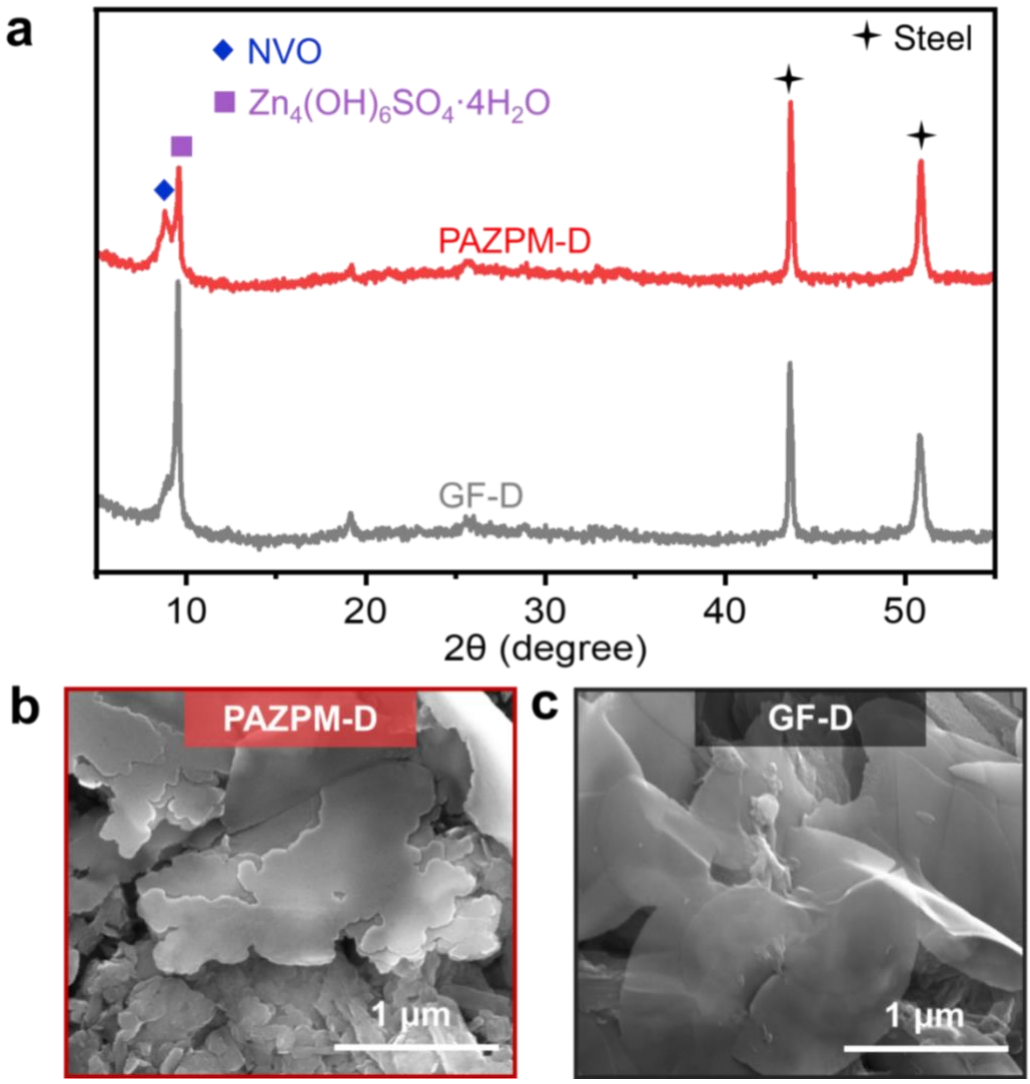

Figure S37. (a) XRD patterns and (b, c) SEM images of NVO cathodes in the discharged state using the Janus PAZPM electrolyte (PAZPM-D) and a GF separator filled with 1 M $ZnSO_4$ aqueous solution (GF-D).

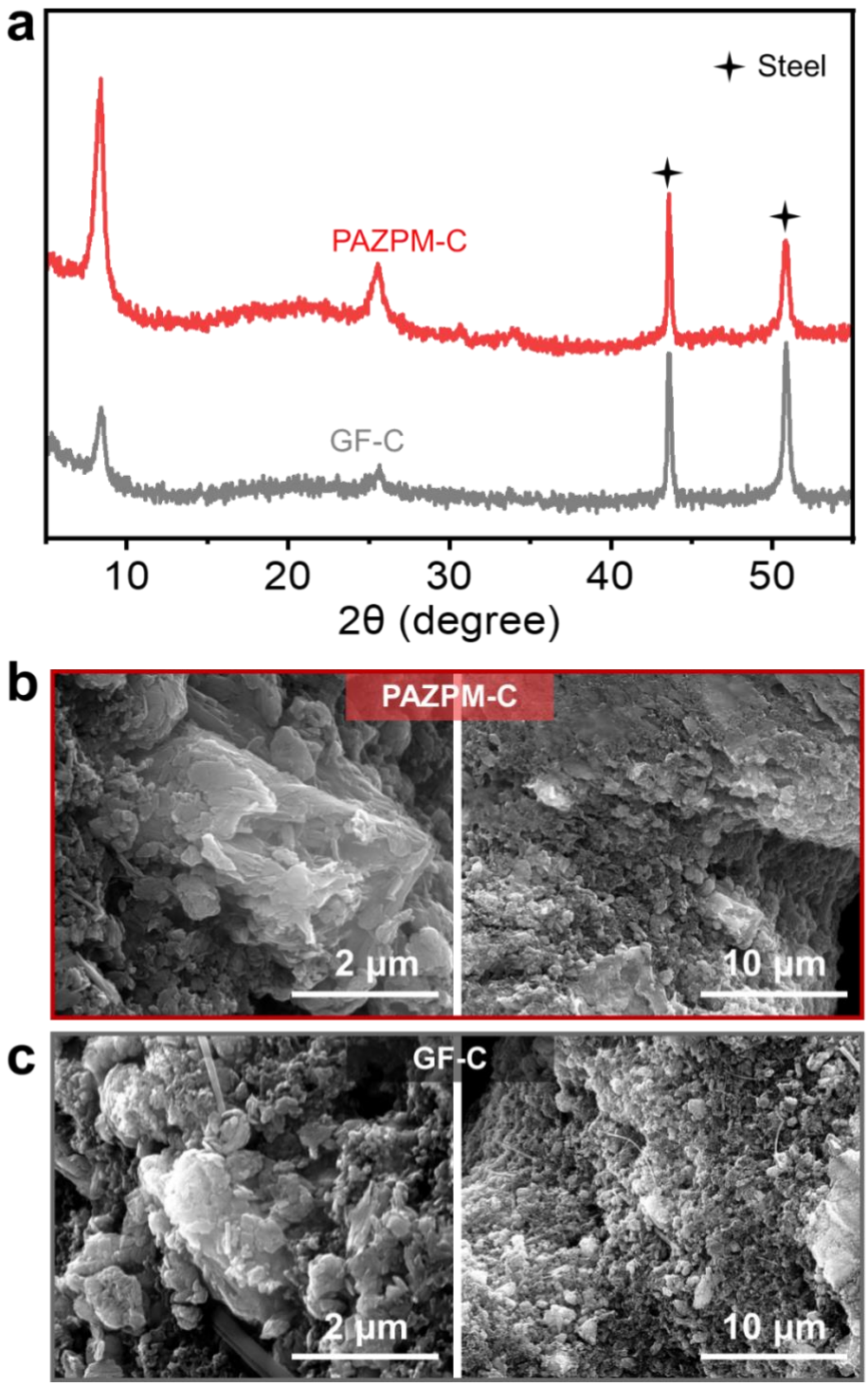

Figure S38. (a) XRD patterns and (b, c) SEM images of NVO cathodes in the fully charged state using the Janus PAZPM electrolyte (PAZPM-C) and a GF separator filled with 1 M $ZnSO_4$ aqueous solution (GF-C).

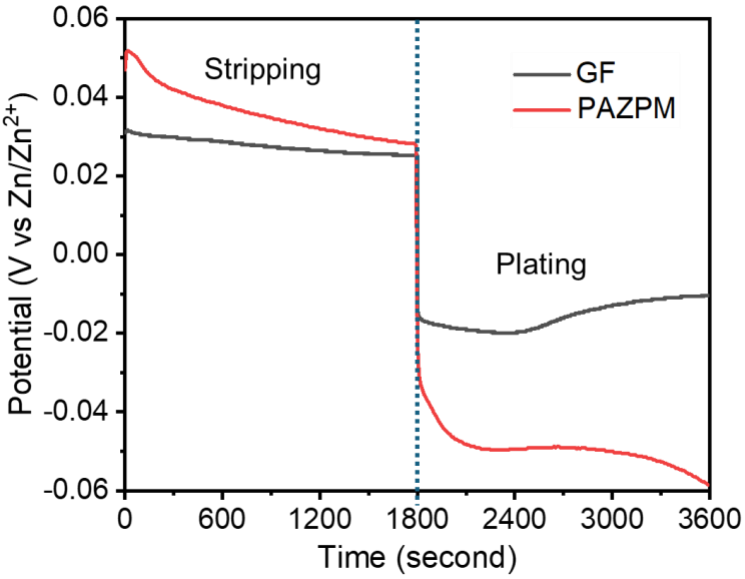

Figure S39. The stripping/plating process of Zn anode in Janus PAZPM hydrogel and GF using three-electrode system with Zn foils as the working electrode and counter electrode, together with Zn ring as the reference electrode.

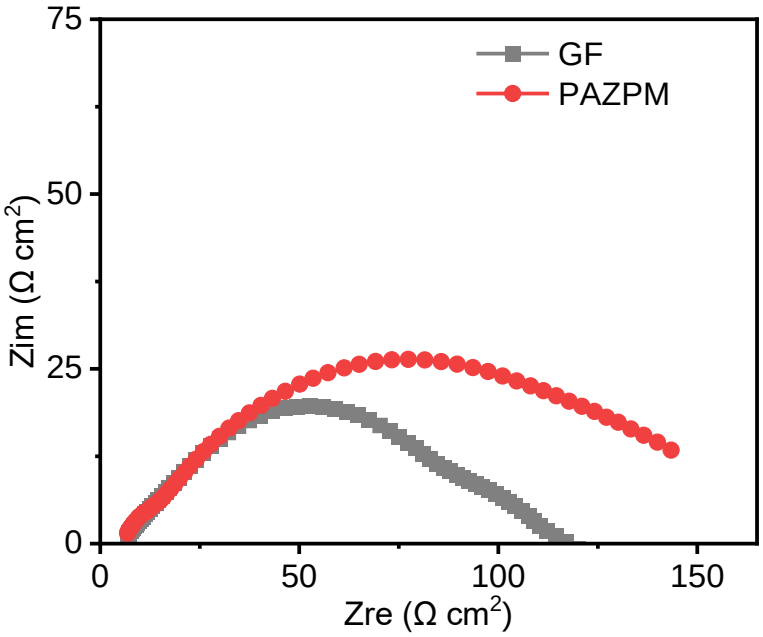

Figure S40. EIS spectra at the OCV for the Zn anode using three electrode cells (working electrode: Zn foil; reference electrode: Zn ring; counter electrode: Zn foil) with the Janus PAZPM hydrogel electrolyte and a GF separator filled with 1 M $ZnSO_4$ aqueous electrolyte.

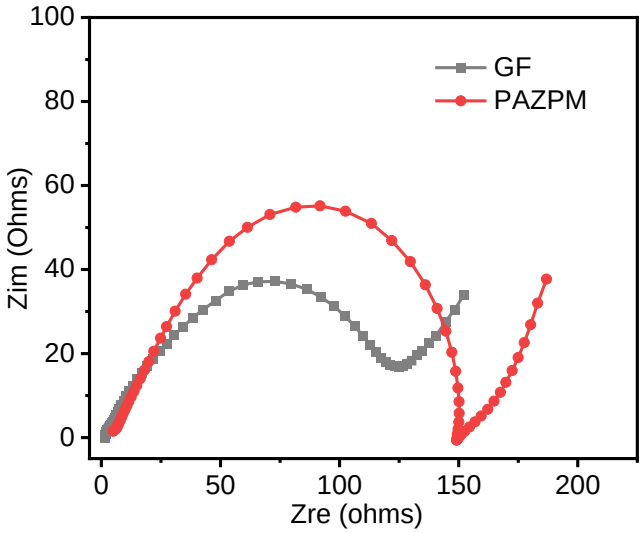

Figure S41 EIS spectra at the open circuit voltage (OCV) state for Zn||NVO cell in two electrode systems using electrolytes of GF filled with $ZnSO_4$ aqueous solution and Janus PAZPM hydrogel.

In Figure S41, the EIS spectra of Zn||NVO coin-type cells employing GF and Janus PAZPM hydrogel electrolyte were compared. Similar to the analysis conducted on three-electrode systems (Figure S35 and S40), the Zn||NVO cell in a two-electrode system utilizing Janus PAZPM hydrogel electrolyte (148 Ω) exhibits higher charge transfer resistance compared to that using GF (124 Ω). This difference can be attributed to the lower water amount on the Zn anode side and the presence of strong hydrogen bonds on the cathode side in the Janus PAZPM hydrogel electrolyte. However, as illustrated in Figure 2h, Zn||NVO cells using Janus hydrogel demonstrate significantly higher rate capabilities than those using GF. Through our comparison experiments, the improved rate capabilities observed with Janus hydrogel should be attributed to the high reversibility of ion-insertion/extraction and stability of NVO cathodes using the Janus hydrogel (as depicted in Figure 2b-2g).

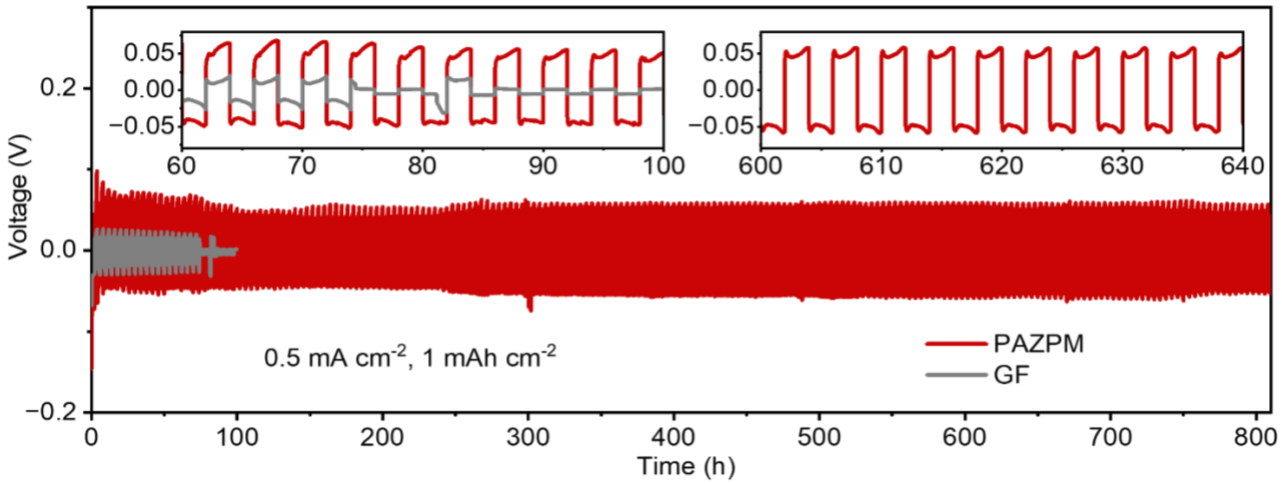

Figure S42. Long-term cycling performances of Zn||Zn symmetric cells at a current density of 0.5 mA cm^{-2} and a capacity of 1 mAh cm^{-2}.

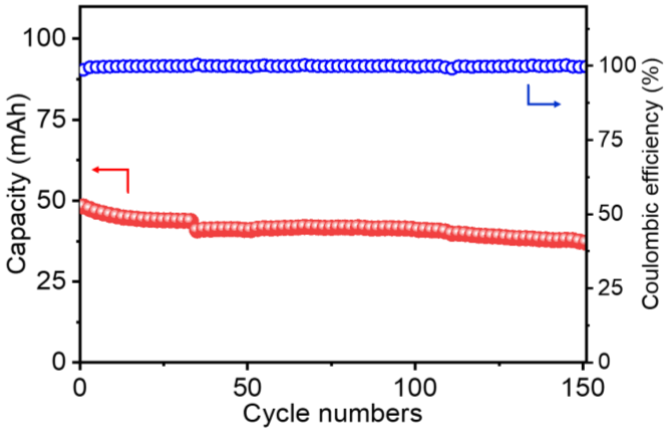

Figure S43. Cycling performance of the Zn||NVO pouch cell with the Janus PAZPM hydrogel electrolyte and 50-μm Zn foil.

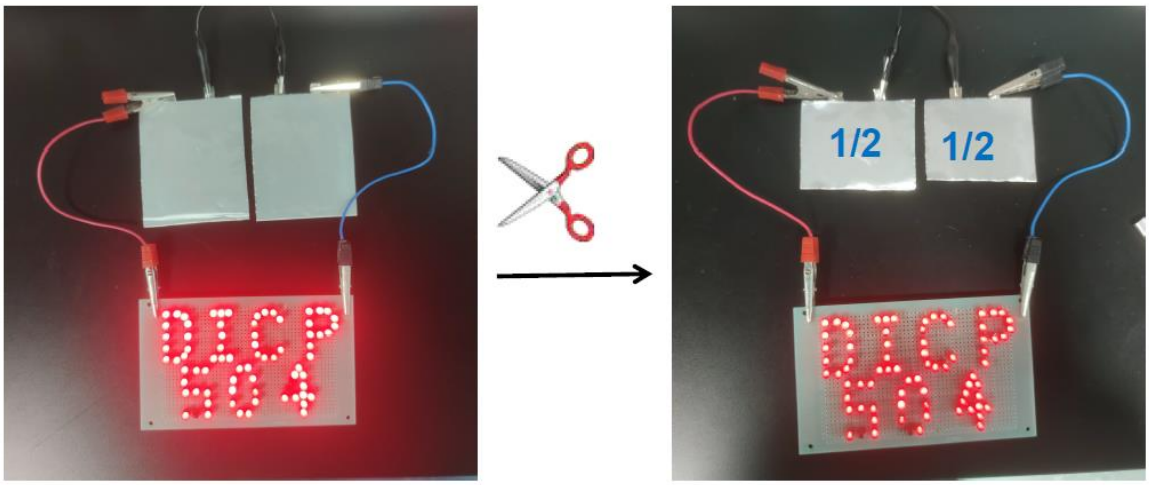

Figure S44. Durability demonstration of the Zn||NVO pouch cells with Janus PAZPM hydrogel electrolyte for powering LEDs while cutting.

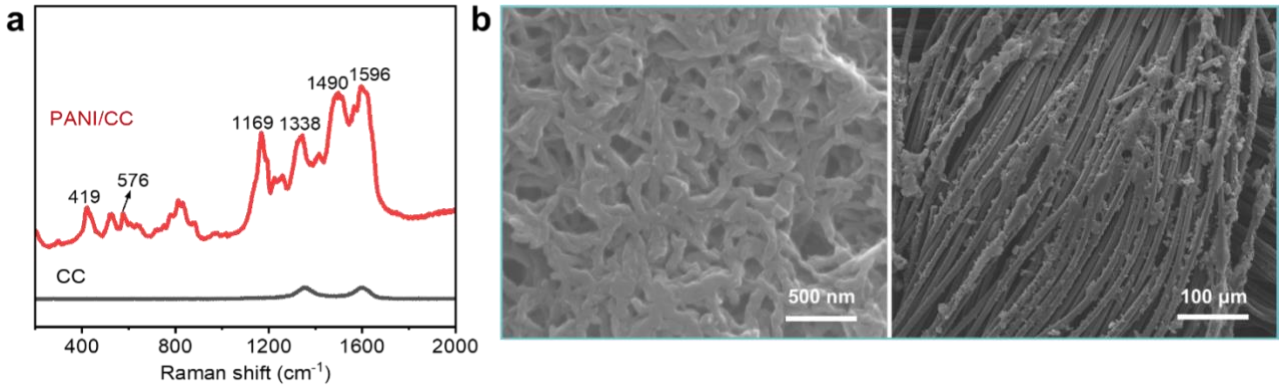

Figure S45. (a) Raman spectra of PANI/CC and CC. (b) SEM images of the PANI/CC cathode.

In Figure S45a, the peak at 1596 cm^{-1} was assigned to the C-C stretching vibrations of benzenoid units. The band at 1490 cm^{-1} was attributed to the C=N stretching vibrations of quinoid diimine units. The characteristic peak at 1338 cm^{-1} was assigned to the stretching vibrations of the C-$N^{\cdot+}$ stretching vibration. The peak at 1169 cm^{-1} was related to the C-H bending of the benzoid. The peak at 576 cm^{-1} is attributed to the vibrational modes of the cyclized structures. The region at 419 cm^{-1} is attributed to C-N-C torsion.[3,4]

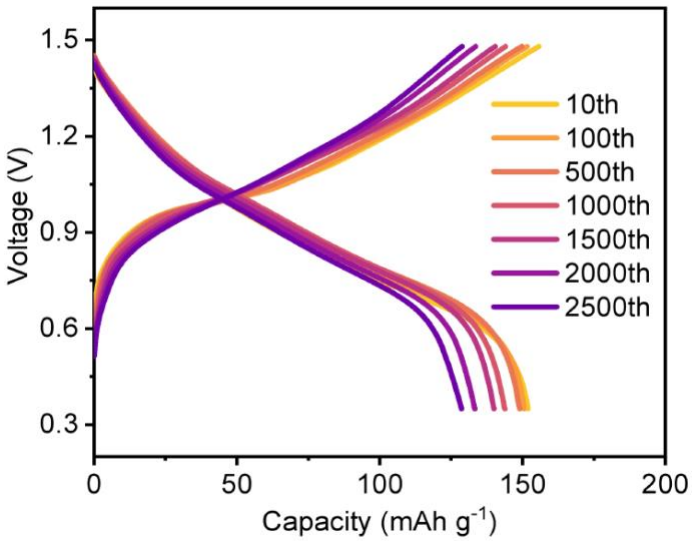

Figure S46. Galvanostatic charge/discharge profiles after certain cycles of Zn||PANI full cells using the Janus PAZPM hydrogel electrolyte at 2 A g^{-1}.

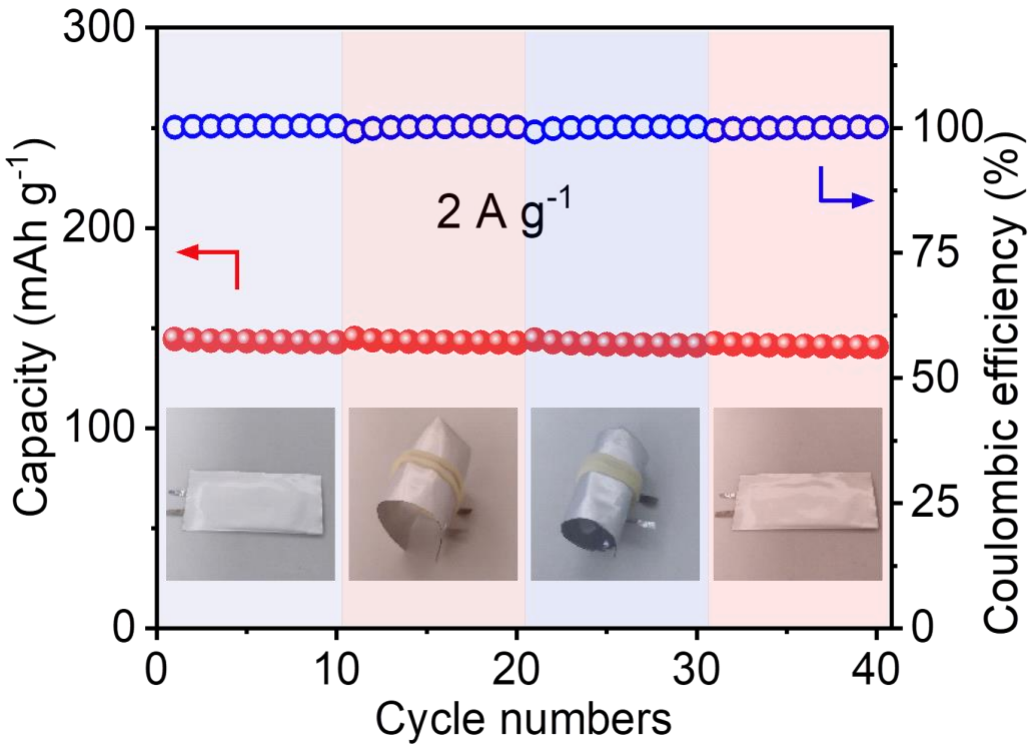

Figure S47. Cycling performances of the Zn||PANI full cells prepared using the Janus PAZPM hydrogel electrolyte under different bending conditions.

Table S1. The monomer proportions used for the preparation of Janus and symmetric PAZPM.

	AM (%)	NIPAM (%)	Zn-AC (%)	MBAA (%)
Janus PAZPM/15%-PAZPM	79.7	15	5	0.3
symmetric P-PAZPM	79.7	15	5	0.3
symmetric G-PAZPM	79.7	15	5	0.3
Janus 0%-PAZPM	94.7	0	5	0.3
Janus 5%-PAZPM	89.7	5	5	0.3
Janus 25%-PAZPM	69.7	25	5	0.3

Table S2. The monomer weights used for the preparation of Janus and symmetric PAZPM.

	AM (g)	NIPAM (g)	Zn-AC (g)	MBAA (g)
Janus PAZPM/15%-PAZPM	0.2842	0.0849	0.0519	0.0023
symmetric P-PAZPM	0.2842	0.0849	0.0519	0.0023
Symmetric G-PAZPM	0.2842	0.0849	0.0519	0.0023
Janus 0%-PAZPM	0.3375	0	0.0519	0.0023
Janus 5%-PAZPM	0.3198	0.0282	0.0519	0.0023
Janus 25%-PAZPM	0.2487	0.1415	0.0519	0.0023

Table S3. The performance comparison of Zn||NVO full cells using our Janus and symmetric hydrogel electrolytes in this work, and some representative zinc ion batteries using NH_4^+ preinserted V_2O_5 cathodes in previous references.

Cathode material	Electrolyte	Cycle performance	Ref.
$(NH_4)_2V_{10}O_{25}\cdot 8H_2O$	1 M $ZnSO_4$ aqueous solution/Janus PAZPM	472 mAh g^{-1} at 0.5 A g^{-1} 87% retained after 100 cycles at 0.5 A g^{-1} 307 mAh g^{-1} at 5 A g^{-1} 88% retained after 1000 cycles at 5 A g^{-1}	This work
$(NH_4)_2V_{10}O_{25}\cdot 8H_2O$	1 M $ZnSO_4$ aqueous solution/glass fiber	455 mAh g^{-1} at 0.5 A g^{-1} 25% retained after 100 cycles at 0.5 A g^{-1} 274 mAh g^{-1} at 5 A g^{-1} 26% retained after 1000 cycles at 5 A g^{-1}	This work
$(NH_4)_2V_{10}O_{25}\cdot 8H_2O$	1 M $ZnSO_4$ aqueous solution/ symmetric G- PAZPM	447 mAh g^{-1} at 0.5 A g^{-1} 56% retained after 100 cycles at 0.5 A g^{-1}	This work
$(NH_4)_2V_{10}O_{25}\cdot 8H_2O$	1 M $ZnSO_4$ aqueous solution/ symmetric P- PAZPM	470 mAh g^{-1} at 0.5 A g^{-1} 34% retained after 100 cycles at 0.5 A g^{-1}	This work
NH_4^+-V_2O_5	3 M $Zn(CF_3SO_3)_2$ aqueous electrolyte/filter paper	151 mAh g^{-1} at 10 A g^{-1} 78.2% retained after 3600 cycles at 10 A g^{-1}	5
hydrated ammonium vanadate nanosheets	3 M $Zn(CF_3SO_3)_2$ aqueous electrolyte/glass fiber	183 mAh g^{-1} at 2 A g^{-1} 85% retained after 1000 cycles at 2 A g^{-1} 121 mAh g^{-1} at 0.2 A g^{-1} 75% retained after 50 cycles at 0.2 A g^{-1} 60 mAh g^{-1} at 1 A g^{-1} 87% retained after 1000 cycles at 1 A g^{-1}	6
$(NH_4)_2V_4O_9$	3 M $Zn(CF_3SO_3)_2$ aqueous electrolyte/glass fiber	105 mAh g^{-1} at 5 A g^{-1} 71% retained after 1000 cycles at 5 A g^{-1}	7
poly(3,4-ethylenedioxythiophene) (PEDOT)-vanadium pentoxide (V_2O_5)	3 M $Zn(OTF)_2$ aqueous solution/ glass fiber	396 mAh g^{-1} at 2 A g^{-1} 40% retained after 1000 cycles at 2 A g^{-1}	8
Defective $(NH_4)_2V_{10}O_{25}\cdot 8H_2O$	3 M $Zn(CF_3SO_3)_2$ aqueous electrolyte/glass fiber	327 mAh g^{-1} at 5 A g^{-1} 29% retained after 1000 cycles at 5 A g^{-1}	9

$(NH_4)_{0.37}V_2O_5 \cdot 0.15 H_2O$	2 M $ZnSO_4$ aqueous solution/glass wool	398 mAh g^{-1} at 0.5 A g^{-1} 90% retained after 50 cycles at 0.5 A g^{-1} 168 mAh g^{-1} at 10 A g^{-1} 84% retained after 1000 cycles at 10 A g^{-1}	10
$(NH_4)_xV_2O_5 \cdot nH_2O$	1 M $ZnSO_4$ aqueous electrolyte/glass fiber	171 mAh g^{-1} at 0.2 A g^{-1} 68% retained after 100 cycles at 0.2 A g^{-1}	11
sulfur-doped $(NH_4)_2V_{10}O_{25} \cdot 8H_2O$	3 M $Zn(CF_3SO_3)_2$ aqueous solution/glass fiber	323 mAh g^{-1} at 0.5 A g^{-1} 62% retained after 100 cycles at 0.5 A g^{-1} 189 mAh g^{-1} at 5 A g^{-1} 38.9% retained after 100 cycles at 5 A g^{-1}	12
$(NH_4)_xV_2O_5 \cdot nH_2O$	1 M $ZnSO_4$ aqueous solution/glass fiber	258 mAh g^{-1} at 2 A g^{-1} 53% retained after 400 cycles at 2 A g^{-1}	13
$NH_4V_4O_{10}$	3 M $Zn(CF_3SO_3)_2$ aqueous solution/glass fiber	227 mAh g^{-1} at 4 A g^{-1} 66 % retained after 1000 cycles at 4 A g^{-1} 363.3 mAh g^{-1} at 0.2 A g^{-1} 52.2 % retained after 100 cycles at 0.2 A g^{-1}	14
F-doped $NH_4V_4O_{10}$	3 M $Zn(CF_3SO_3)_2$ aqueous solution/glass fiber	450 mAh g^{-1} at 0.2 A g^{-1} 80.7% retained after 100 cycles at 2 A g^{-1}	14
$(NH_4)_{0.38}V_2O_5$/CNs	2M $ZnSO_4$ aqueous solution/glass fiber	254 mAh g^{-1} at 2 A g^{-1} 80.3% retained after 500 cycles at 2 A g^{-1} 103 mAh g^{-1} at 10 A g^{-1} 40.4% retained after 500 cycles at 10 A g^{-1}	15
$NH_4V_4O_{10}$	2M $ZnSO_4$ aqueous solution/glass fiber	294 mAh g^{-1} at 5 A g^{-1} 68% retained after 1200 cycles at 5 A g^{-1}	16
V_2O_5	2M $ZnSO_4$ aqueous solution/glass fiber	110 mAh g^{-1} at 2.5 A g^{-1} 56% retained after 1200 cycles at 2.5 A g^{-1}	17
$NH_4V_4O_{10}$	2M $ZnSO_4$ aqueous solution/glass fiber	233 mAh g^{-1} at 1 A g^{-1} 43% retained after 500 cycles at 1 A g^{-1} 124 mAh g^{-1} at 3 A g^{-1} 27% retained after 1000 cycles at 3 A g^{-1}	18
$NH_4V_4O_{10}$	2M $ZnSO_4$ aqueous solution/ chitosan cross-linked with polyacrylamide	216 mAh g^{-1} at 1 A g^{-1} 82% retained after 500 cycles at 1 A g^{-1} 114 mAh g^{-1} at 3 A g^{-1}	18

		57% retained after 1000 cycles at 3 A g^{-1}	
$NH_4V_4O_{10}$	2M $ZnSO_4$ aqueous solution/ sulfonated chitosan cross-linked with polyacrylamide	209 mAh g^{-1} at 1 A g^{-1} 96.1% retained after 500 cycles at 1 A g^{-1} 118 mAh g^{-1} at 3 A g^{-1} 80% retained after 1000 cycles at 3 A g^{-1}	18
$V_2O_5 \cdot nH_2O$/CNT	2 M $ZnSO_4$ aqueous solution/gelatin	185 mAh g^{-1} at 2 A g^{-1} 35% retained after 200 cycles at 2 A g^{-1}	19
proton-doped magnesium vanadium oxide (HMgVO)	2 M $ZnSO_4$ + 0.1 M $MnSO_4$ aqueous solution/ polyacrylamide/carboxymethyl cellulose/gelatin (PCG)	225 mAh g^{-1} at 1 A g^{-1} 52 % retained after 1000 cycles at 1 A g^{-1} 225 mAh g^{-1} at 1 A g^{-1} 72% retained after 100 cycles at 1 A g^{-1}	20
poly(3,4-ethylenedioxythiophene) (PEDOT)-vanadium pentoxide (V_2O_5) (PVO)	3 M $Zn(OTF)_2$ aqueous solution/ dried composite hydrogel with Fe^{3+} ionic crosslinks (CH/D/Fe)	350 mAh g^{-1} at 2 A g^{-1} 74% retained after 1000 cycles at 2 A g^{-1}	8
V_2O_5	2 M $ZnSO_4$ aqueous solution/ xanthan gum with Hex-agonal boron nitride nanosheets	363 mAh g^{-1} at 2 A g^{-1} 72 % retained after 1000 cycles at 2 A g^{-1}	21
$Mg_{0.23}V_2O_5 \cdot 1.0H_2O$	1 M $Zn(CF_3SO_3)_2$ aqueous solution/cellulose nanofiber (CNF)‑polyacrylamide	367 mAh g^{-1} at 0.5 A g^{-1} 85% retained after 100 cycles at 0.5 A g^{-1} 253 mAh g^{-1} at 5 A g^{-1} 83% retained after 1000 cycles at 5 A g^{-1}	22
$NH_4V_4O_{10}$	2 M $ZnSO_4$ aqueous solution/ tannic acid (TA) modified sodium alginate (SA) composite gel	293 mAh g^{-1} at 0.5 A g^{-1} 78% retained after 100 cycles at 0.5 A g^{-1}	23
$NH_4V_4O_{10}$	2 M $ZnSO_4$ aqueous solution/ sodium alginate (SA) composite gel	321 mAh g^{-1} at 0.5 A g^{-1} 64% retained after 100 cycles at 0.5 A g^{-1}	23
V_2O_5	3 M $ZnSO_4$ aqueous solution/cellulose-based hydrogel membrane	400 mAh g^{-1} at 0.1 A g^{-1} 62.5% retained after 200 cycles at 0.1 A g^{-1} 400 mAh g^{-1} at 0.1 A g^{-1}	24

		77% retained after 100 cycles at 0.1 A g^{-1}	
V_2O_5/ CNT	2 M $ZnSO_4$ aqueous solution/ multi-ion conducting P(iota carrageenan - acrylamide)	334.8 mAh g^{-1} at 0.2 A g^{-1} 36% retained after 150 cycles at 0.2 A g^{-1} 162 mAh g^{-1} at 0.5 A g^{-1} 80% retained after 100 cycles at 0.5 A g^{-1}	25
NH_4^+-deficient $NH_4V_4O_{10}$	3 M $Zn(CF_3SO_3)_2$ aqueous solution/ polyacrylamide	466 mAh g^{-1} at 0.1 A g^{-1} 71% retained after 100 cycles at 0.1 A g^{-1} 300 mAh g^{-1} at 5 A g^{-1} 88% retained after 1000 cycles at 5 A g^{-1}	26
V_2O_5	2 M $Zn(CF_3SO_3)_2$ aqueous solution/polyacrylamide-based supramolecular hydrogel (PAM-Hbimcp-Zn)	230.6 mAh g^{-1} at 2 A g^{-1} 75.2% retained after 1000 cycles at 2 A g^{-1}	27
$V_2O_5 \cdot 1.6H_2O$	2 M $ZnSO_4$ aqueous solution/polyacrylamide-poly (ethylene glycol) diacrylate-carboxymethyl cellulose (PMC) hydrogel	380.74 mAh g^{-1} at 1 A g^{-1} 71.1% retained after 500 cycles at 1 A g^{-1} 380.74 mAh g^{-1} at 1 A g^{-1} 89% retained after 100 cycles at 1 A g^{-1}	28
VO_2	1 M $Zn(CF_3SO_3)_2$ aqueous solution/polyacrylamide-chitin nanofiber (PAM-ChNF) hydrogel	144.7 mAh g^{-1} at 5 A g^{-1} 86% retained after 600 cycles at 5 A g^{-1}	29
La-V_2O_5	1 M $Zn(CF_3SO_3)_2$ aqueous solution/polyacrylamide	68 mAh g^{-1} at 5 A g^{-1} 73.4% retained after 1000 cycles at 5 A g^{-1}	30

Table S4. The performance comparison of Zn||Zn symmetric cells using Janus hydrogel electrolytes in this work, and some representative hydrogel electrolytes reported in previous references.

Electrolyte	Cycle time	Ref.
1 M $ZnSO_4$ aqueous solution/Janus PAZPM	3600 hours (0.5 mA cm^{-2}, 0.25 mAh cm^{-2}) 1700 hours (4 mA cm^{-2}, 2 mAh cm^{-2})	This work
1 M $ZnSO_4$ aqueous solution/glass fiber	308 hours (0.5 mA cm^{-2}, 0.25 mAh cm^{-2}) 62 hours (4 mA cm^{-2}, 2 mAh cm^{-2})	This work
2M $ZnSO_4$ aqueous solution/ sulfonated chitosan cross-linked with polyacrylamide (PAM)	2600 hours (1 mA cm^{-2}, 1 mAh cm^{-2}) 400 hours (3 mA cm^{-2}, 3 mAh cm^{-2})	18
2M $ZnSO_4$ aqueous solution/ chitosan cross-linked with PAM	500 hours (1 mA cm^{-2}, 1 mAh cm^{-2})	18
3M $ZnSO_4$ aqueous solution/ Na-montmorillonite-PAM	300 hours (0.5 mA cm^{-2}, 0.25 mAh cm^{-2})	31
3M $ZnSO_4$ aqueous solution/ PAM	197 hours (0.5 mA cm^{-2}, 0.25 mAh cm^{-2})	31
2 M $ZnSO_4$ + 0.1 M $MnSO_4$ aqueous solution/ polyacrylamide/carboxymethyl cellulose/gelatin (PCG)	1100 hours (0.1 mA cm^{-2}, 0.1 mAh cm^{-2})	20
3 M $Zn(OTF)_2$ aqueous solution/ dried composite hydrogel with Fe^{3+} ionic crosslinks (CH/D/Fe)	600 hours (1 mA cm^{-2}, 1 mAh cm^{-2})	8
2 M $ZnSO_4$ aqueous solution/ xanthan gum hydrogel with Hex-agonal boron nitride nanosheets	1500 hours (2 mA cm^{-2}, 2 mAh cm^{-2})	21
2 M $ZnSO_4$ aqueous solution/ xanthan gum hydrogel	400 hours (2 mA cm^{-2}, 2 mAh cm^{-2})	21
3 M $ZnSO_4$ aqueous solution/cellulose-based hydrogel membrane	1800 hours (1 mA cm^{-2}, 1 mAh cm^{-2})	24
2 M $ZnSO_4$ aqueous solution/P(iota carrageenan - acrylamide)	400 hours (0.25 mA cm^{-2}, 0.125 mAh cm^{-2})	25

2 M $Zn(CF_3SO_3)_2$ aqueous solution/polyacrylamide-based supramolecular hydrogel	500 hours (1 mA cm^{-2}, 1 mAh cm^{-2})	27
polymeric single-ion conductor (PSIC)-based p(Zinc 5-(Methacrylamido)tetrazolate) electrolytes	1500 hours (0.5 mA cm^{-2}, 0.5 mAh cm^{-2}) 550 hours (1 mA cm^{-2}, 1 mAh cm^{-2})	32

Movie S1.

Contact angle measurement of a $ZnSO_4$ (1 M) aqueous solution on a glass fibre separator.

References and Notes

1. M. J. Frisch, G. W. Trucks, H. B. Schlegel, G. E. Scuseria, M. A. Robb, J. R. Cheeseman, G. Scalmani, V. Barone, G. A. Petersson, H. Nakatsuji, X. Li, M. Caricato, A. V. Marenich, J. Bloino, B. G. Janesko, R. Gomperts, B. Mennucci, H. P. Hratchian, J. V. Ortiz, A. F. Izmaylov, J. L. Sonnenberg, Williams, F. Ding, F. Lipparini, F. Egidi, J. Goings, B. Peng, A. Petrone, T. Henderson, D. Ranasinghe, V. G. Zakrzewski, J. Gao, N. Rega, G. Zheng, W. Liang, M. Hada, M. Ehara, K. Toyota, R. Fukuda, J. Hasegawa, M. Ishida, T. Nakajima, Y. Honda, O. Kitao, H. Nakai, T. Vreven, K. Throssell, J. A. Montgomery Jr., J. E. Peralta, F. Ogliaro, M. J. Bearpark, J. J. Heyd, E. N. Brothers, K. N. Kudin, V. N. Staroverov, T. A. Keith, R. Kobayashi, J. Normand, K. Raghavachari, A. P. Rendell, J. C. Burant, S. S. Iyengar, J. Tomasi, M. Cossi, J. M. Millam, M. Klene, C. Adamo, R. Cammi, J. W. Ochterski, R. L. Martin, K. Morokuma, O. Farkas, J. B. Foresman, D. J. Fox, Wallingford, CT, 2016.

2. K. Zhu, T. Wu and K. Huang, *Chem. Mater.*, 2021, **33**, 4089-4098.

3. M. Cochet, G. Louarn, S. Quillard, J.P. Buisson and S. Lefrant, *Part II. J. Raman Spectrosc.*, 2000, **31**, 1041-1049.

4. J.E. Pereira da Silva, D. L. de Faria, A., S. I. Córdoba de Torresi and M. L. A. Temperini, *Macromolecules*, 2000, **33**, 3077-3083.

5. Y. Wang, S. Wei, Z.-H. Qi, S. Chen, K. Zhu, H. Ding, Y. Cao, Q. Zhou, C. Wang, P. Zhang, X. Guo, X. Yang, X. Wu and L. Song, *Proc. Natl. Acad. Sci. U.S.A.*, 2023, **120**, e2217208120.

6. H. Jiang, Y. Zhang, Y. Liu, J. Yang, L. Xu, P. Wang, Z. Gao, J. Zheng, C. Meng and Z. Pan, *J. Mater. Chem. A*, 2020, **8**, 15130-15139.

7. G. Li, Y. Su, S. Zhou, J. Shen, D. Liu, S. Lv, J. Wang, W. Yu, X. Dong and X. Wang, *Chem. Eng. J.*, 2023, **469**, 143816.

8. K. H. Shin, D. Ji, J. M. Park, Y. S. Joe, H. S. Park and J. Kim, *Adv. Funct. Mater.*, 2023, **34**, 2309048.

9. J. Qi, Y. Zhang, M. Li, H. Xu, Y. Zhang, J. Wen, H. Zhai, W. Yang, C. Li, H. Wang, X. Fan and J. Liu, *J. Colloid Interface Sci.*, 2023, **642**, 430-438.

10. M. Tamilselvan, T. V. M. Sreekanth, K. Yoo and J. Kim, *J. Ind. Eng. Chem.*, 2021, **93**, 176-185.

11. L. Xu, Y. Zhang, J. Zheng, H. Jiang, T. Hu and C. Meng, *Mater. Today Energy*, 2020, **18**, 100509.

12. J. Zhang, R. Liu, C. Huang, C. Dong, L. Xu, L. Yuan, S. Lu, L. Wang, L. Zhang and L. Chen, *Nano Energy*, 2024, **122**, 109301.

13. H. Zhao, Q. Fu, D. Yang, A. Sarapulova, Q. Pang, Y. Meng, L. Wei, H. Ehrenberg, Y. Wei, C. Wang and G. Chen, *ACS Nano*, 2020, **14**, 11809-11820.

14. Y. Zhuang, Q. Zong, Y. Wu, C. Liu, Q. Zhang, D. Tao, J. Zhang, J. Wang and G. Cao, *Small*, 2023, 2306561.

15. Y. Jiang, Z. Wu, F. Ye, R. Pang, L. Zhang, Q. Liu, X. Chang, S. Sun, Z. Sun and L. Hu, *Energy Stor. Mater.*, 2021, **42**, 286-294.

16. D. Xu, B. Chen, X. Ren, C. Han, Z. Chang, A. Pan and H. Zhou, *Energy Environ. Sci.*, 2024, **17**, 642-654.

17. L. Han, Y. Guo, F. Ning, X. Liu, J. Yi, Q. Luo, B. Qu, J. Yue, Y. Lu and Q. Li, *Adv. Mater.*, 2023, 2308086.

18. Y. Hu, Z. Wang, Y. Li, P. Liu, X. Liu, G. Liang, D. Zhang, X. Fan, Z. Lu and W. Wang, *Chem. Eng. J.*, 2024, **479**, 147762.

19. Y. Lu, T. Zhu, N. Xu and K. Huang, *ACS Appl. Energy Mater.*, 2019, **2**, 6904-6910.

20. C. Jia, X. Zhang, S. Liang, Y. Fu, W. Liu, J. Chen, X. Liu and L. Zhang, *J. Power Sources*, 2022, **548**, 232072.

21. H. Wang, A. Zhou, Z. Hu, X. Hu, F. Zhang, Z. Song, Y. Huang, Y. Cui, Y. Cui, L. Li, F. Wu and R. Chen, *Angew. Chem. Int. Ed.*, 2024, e202318928.

22. W. Xu, C. Liu, Q. Wu, W. Xie, W.-Y. Kim, S.-Y. Lee and J. Gwon, *J. Mater. Chem. A*, 2020,

8, 18327-18337.

23. B. Zhang, L. Qin, Y. Fang, Y. Chai, X. Xie, B. Lu, S. Liang and J. Zhou, *Sci. Bull.*, 2022, **67**, 955-962.

24. Z. Zheng, S. Yan, Y. Zhang, X. Zhang, J. Zhou, J. Ye and Y. Zhu, *Chem. Eng. J.*, 2023, **475**, 146314.

25. C. Y. Chan, Z. Wang, Y. Li, H. Yu, B. Fei and J. H. Xin, *ACS Appl. Mater. Interfaces*, 2021, **13**, 30594-30602.

26. L. Chen, H. Yue, Z. Zhang, Y. Ma, Y. Wang, M. Xu, Y. Huang and G. Yuan, *Chem. Eng. J.*, 2023, **455**, 140679.

27. Z. J. Chen, T. Y. Shen, M. H. Zhang, X. Xiao, H. Q. Wang, Q. R. Lu, Y. L. Luo, Z. Jin and C. H. Li, *Adv. Funct. Mater*, 2024, 2314864.

28. P. Lin, J. Cong, J. Li, M. Zhang, P. Lai, J. Zeng, Y. Yang and J. Zhao, *Energy Stor. Mater.*, 2022, **49**, 172-180.

29. C. Liu, W. Xu, C. Mei, M. Li, W. Chen, S. Hong, W. Y. Kim, S. y. Lee and Q. Wu, *Adv. Energy Mater.*, 2021, **11**, 2003902.

30. H. Xia, G. Xu, X. Cao, C. Miao, H. Zhang, P. Chen, Y. Zhou, W. Zhang and Z. Sun, *Adv. Mater.*, 2023, **35**, 2301996.

31. S. Ji, J. Qin, S. Yang, P. Shen, Y. Hu, K. Yang, H. Luo and J. Xu, *Energy Stor. Mater.*, 2023, **55**, 236-243.

32. Z. Chen, T. Wang, Y. Hou, Y. Wang, Z. Huang, H. Cui, J. Fan, Z. Pei and C. Zhi, *Adv. Mater.*, 2022, **34**, 2207682.